uc3m | Universidad Carlos III de Madrid

Bioengineering & Aerospace Engineering Department

BACHELOR THESIS

IMPLEMENTATION OF A METAL ARTIFACT REDUCTION METHOD FOR SMALL-ANIMAL CT

Author:

Rodrigo Miri Bertoncini

Director:

Nerea Ballesteros Tenrero

Tutor:

Mónica Abella García

Madrid, September 26th, 2017.

IMPLEMENTATION OF A METAL ARTIFACT REDUCTION METHOD FOR SMALL-ANIMAL CT

Author: Rodrigo Miri Bertoncini

Director: Nerea Ballesteros Tenrero

Tutor: Mónica Abella García

Bioengineering & Aerospace Engineering Department Universidad Carlos III de Madrid

Laboratorio de Imagen Médica (LIM) Hospital General Universitario Gregorio Marañón

ABSTRACT

In the recent years, because of the constantly increasing knew discoveries in the fields of genomics and molecular biology and the development of new technologies, the use of animal models of human diseases has become more frequent. This combined with improvements in biomedical instrumentation and medical imaging has led to the development of micro CT systems enabling noninvasive investigations on animals. The work included in this thesis is framed on one of the lines of research carried out by the Biomedical Imaging and Instrumentation Group (BIIG) from the Bioengineering and Aerospace

Department of Universidad Carlos III de Madrid working jointly with the Gregorio Marañón Hospital. This multidisciplinary group has developed a micro-CT system for small animals, which is used in different preclinical research lines within the group. One of these research lines focuses on the use of brain stimulation as Parkinson disease treatment. Rats have stainless electrodes implanted and fixed with screws in the lateral hypothalamus, through stereotaxic surgery. The CT subsystem of ARGUS is used then to corroborate the surgery was correct and the position of the electrodes is the right one.

The presence of metallic objects creates severe streak artifacts in CT images affecting image quality and hindering the correct representation of anatomy. The beam hardening correction method, already integrated in the ARGUS system results insufficient for the correction of the artifacts derived from the presence of metals. Motivated by this context, the objective of this thesis is to implement an algorithm for metal artifact correction to be included in ARGUS. After reviewing the methods proposed in the literature the one proposed by Meyer et. al. in 2012 was implemented in MATLAB.

The implemented MAR method was evaluated using simulations and real studies acquired with the ARGUS scanner, based on visual assessment, intensity profiles and mean squared error before and after the correction. The results of the evaluation showed an efficient elimination of streaks even for very strong artifact, as it is the case of gold implants. In all cases, bone edges were preserved when correcting with MAR and the metal structures are clearly delimited after correction.

KEYWORDS

X ray, radiography, tomography, metal artifact, 3D image, image reconstruction

INDEX

Index of figures:

Index of tables:

1.INTRODUCTION

Nowadays medical imaging is crucial in diagnosis, medical treatments and investigation. Different imaging modalities are used every day which are classified depending on the kind of radiation used. In each one, the patient is radiated with a specific kind of energy depending on the purpose pursued and the images obtained are a spatial distribution of one or several chemical and physical properties of the radiated body. Five main modalities stand out: magnetic resonance imaging (radio waves), radiology (X-rays), nuclear medicine (gamma rays), echography (ultrasound) and endoscopy (light).

Radiology is the most widely used modality worldwide with multiple applications in diagnosis, radiotherapy or surgery. X ray imaging allows to obtain spatial high-resolution images and the extraction of detailed information about the anatomy of the subject according to the density of the tissue traversed by the rays. It is low cost, easy to perform and very fast to acquire. However, radiology images are obtained using ionizing radiation which brings several risks. The radiated dose must then be kept as low as possible, limiting the use of this modality for everyone but especially for some high-risk population groups such as pregnant women or babies.

1.1 Introduction to X-rays

Wilhem C. Roentgen discovered x-ray radiation unintentionally in 1895 while working with a cathodic ray tube. X rays are a form of electromagnetic radiation whose main feature is to be ionizing; thus having the potential of liberating an electron from the electronic cloud of an atom nucleus. Molecules exposed to ionizing radiation can be broken inducing unwanted chemical reactions in the organism.

X ray energy goes from $5 \cdot 10^3$ to $10^6 \ eV$, being just above ultra violet radiation in the electromagnetic spectrum (see Figure 1-1); this corresponds to wavelengths from 10 to 0.01 nm. In clinical application, energies between $10 \ keV$ and $150 \ keV$ are used.

Due to its high energy, X-rays are more frequently described as a particle than a wave. The energy of an x ray photon is defined by:

$$E = h \cdot \frac{c}{\lambda} = h \cdot f$$

Where $h = 4.135 \cdot 10^{-15} eV \cdot s$ is the Planck's constant, $c = 2.997925 \cdot 10^8 m/s$ is the speed of light, λ is the wave length and f is the frequency.
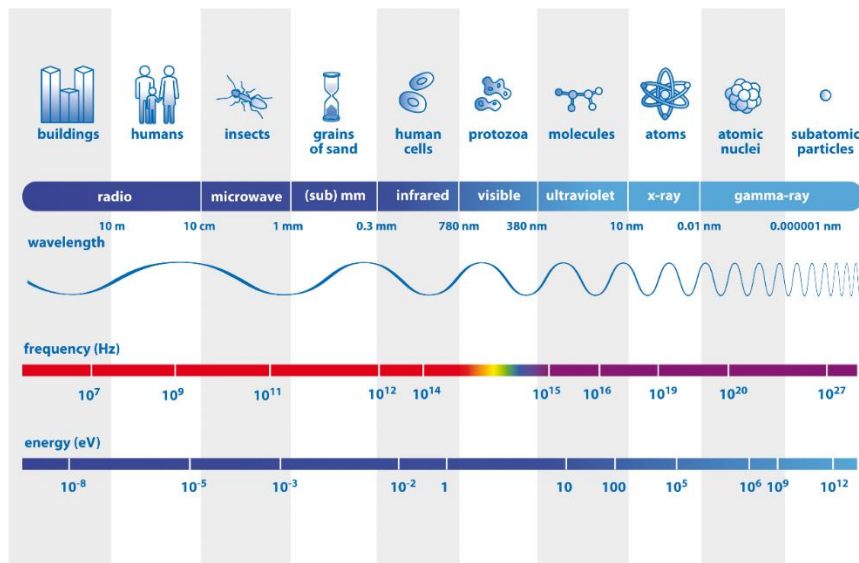
FIGURE 1-1: ELECTROMAGNETIC SPECTRUM AND X-RAY POSITION. SOURCE: [1]

1.2 X ray generation

X rays are produced in a vacuum tube, known as an x ray tube, which contains a cathode, and an anode. The electric current through the cathode releases electrons by thermal excitation, which are accelerated by the high voltage applied between the cathode and the anode, hitting the metal receptor in the anode. The most common metal used for the anode receptor is tungsten although other metals can be used. Only 4% of the energy is transformed into x ray photons, the rest turns into heat. Figures 1-2 and 1-3 show an x ray tube.
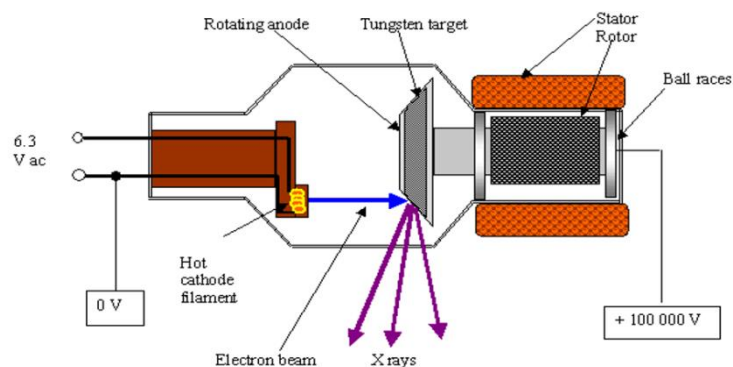
FIGURE 1-2: SKETCH OF AN X-RAY TUBE. [2]

Two different atomic processes generate x rays at the cathode (figure 1-4):

Bremsstrahlung radiation (braking radiation):

When the high energy electrons get the tungsten receptor, they interact with the coulomb field, produced by the nucleus of the atoms of the receptor, undergoing deceleration and changing their trajectory. This liberates part of their kinetic energy in form of x ray photons. The amount of photons generated is inversely proportional to the electron energy as shown in figure 1-5; the lower the energy, the higher the probability of being slowed down.

Characteristic radiation:

It occurs when an accelerated electron happens to ionize one of the anode atoms by kicking out one of his inner shells electron; a vacancy appears in an inner shell of the atom unchaining the jump of electros from outer shells to fill the gap. Those electron transitions generate x-ray photons with the characteristic energy difference between the two layers. As shown in figure 1-5 it is visualized as two pairs of peaks. The first pair corresponding to a lower energy is for k_α transitions, transitions to the K shell from the next shell up (the L shell). The second pair corresponds to higher energy transitions, k_β, when the gap in the K shell is filled with an electron jumping from an outer shell, two or more shells away. The K shell contains 2 electrons and those electrons do not have the exact same energy, this explains the duplicity of this peaks, the energy transition of the electron jump will slightly vary depending on which of the two k shell electrons was ejected. Many times, the double peaks are presented as a single peak neglecting the energy difference.
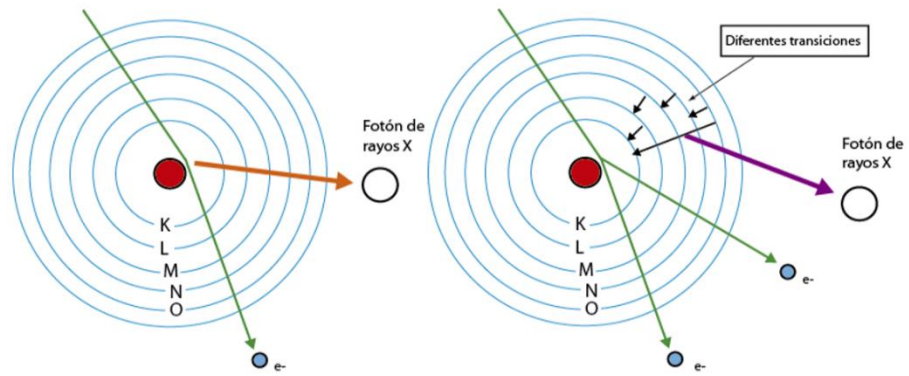
FIGURE 1-4: SKETCH OF THE PROCESSES INVOLVED IN X RAY GENERATION: (LEFT) BREMSSTRAHLUNG AND (RIGHT) CHARACTERISTIC RADIATION
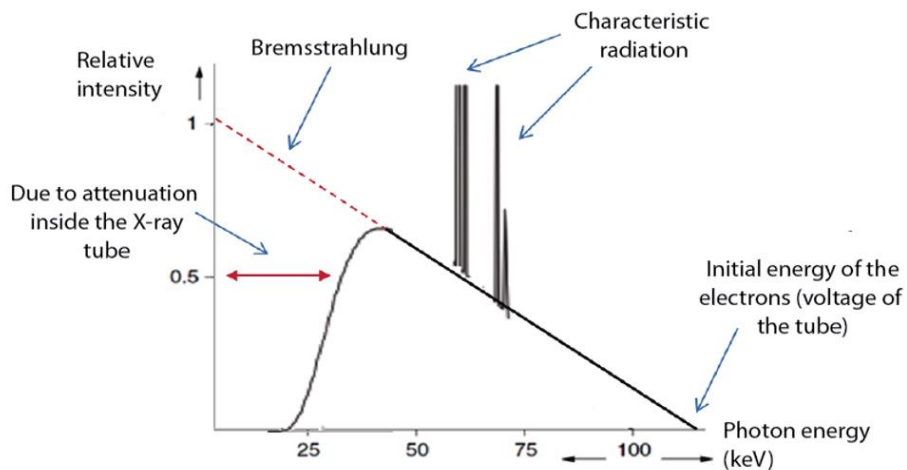
FIGURE 1-5: CHARACTERISTIC FORM OF THE X-RAY EMISSION SPECTRUM DUE TO THE TYPICAL PHENOMENA THAT OCCUR IN THE XRAY TUBE. SOURCE: [4]

The most important parameters in x ray generation are:

- The energy of the emitted photons, that depends on the energy of the electrons hitting the anode which is control by the voltage between the anode and the cathode.

- The amount of emitted photons that depends on the amount of electrons hitting the anode which is proportional to the cathode current and the time the current is on.

4

- The total incident energy in the anode, determine by the product of the cathode current, the voltage between the anode and the cathode, and the time the current is on.

1.3 X rays interaction with matter

For common energy levels used in clinical application (10 - 150 keV) several effects take place when x rays interact with matter:

Photoelectric effect: Occurs when an x ray photon transfers his whole energy to an electron of the radiated sample, in the form of kinetic energy, ejecting him from the atom (Ionization).

Compton effect: Occurs when an x ray photon collides with an electron, generating a photon of lower energy and different trajectory.

Rayleigh effect: Occurs when an x ray photon interacts with the electric field of an electron and gets deviated without changing his energy.

Figure 1-6 and 1-7 summarizes those phenomena:
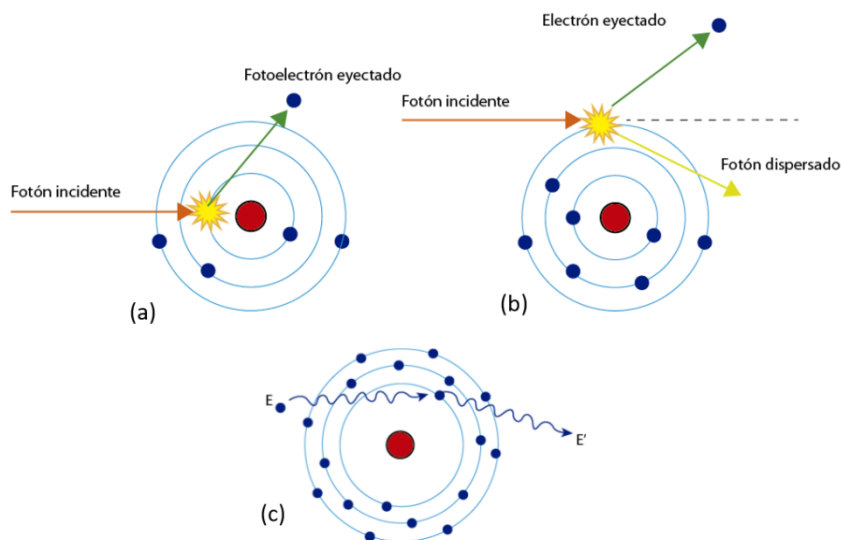
FIGURE 1-6: DIAGRAMS OF THE PROCESSES THAT OCCUR WHEN X-RAY PHOTONS INTERACT WITH MATTER: (A) PHOTOELECTRIC EFFECT, (B) COMPTON EFFECT AND (C) RAYLEIGH EFFECT
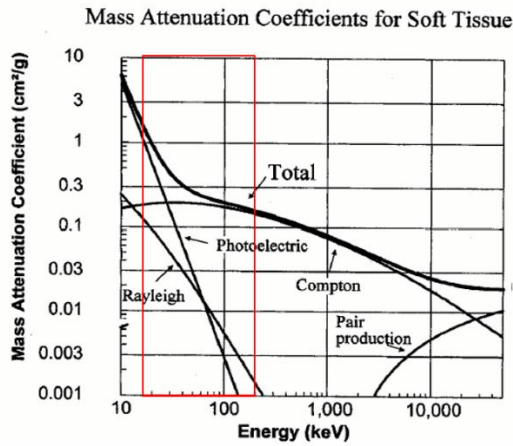
FIGURE 1-7: DIAGRAM OF THE DIFFERENT PHENOMENA PRODUCED BY THE INTERACTING X-RAY PHOTONS WITH SOFT TISSUE (PHOTOELECTRIC EFFECT, COMPTON, RAYLEIGH AND PAIR PRODUCTION) AS A FUNCTION OF THE ENERGY OF THESE PHOTONS. THE RED BOX SHOWS THE ENERGY RANGE (keV) USED IN MEDCIAL IMAGING. SOURCE: [5]

1.4 X rays detection

To produce an image x ray need to be captured and converted into information. First detectors used in medical X rays where based on photographic silver recovery film. However, this film is more sensible to visible light than to x-ray, therefore very high doses where needed to get high quality images. Due to this problem, fluorescent intensifying layers where added in contact with the photographic film. Photon interaction with the fluorescent layer liberated visible light photons that where then detected by the silver recovery film. This way the radiation dose applied to the patient can be reduced for a high-quality image (see figure 1-8)
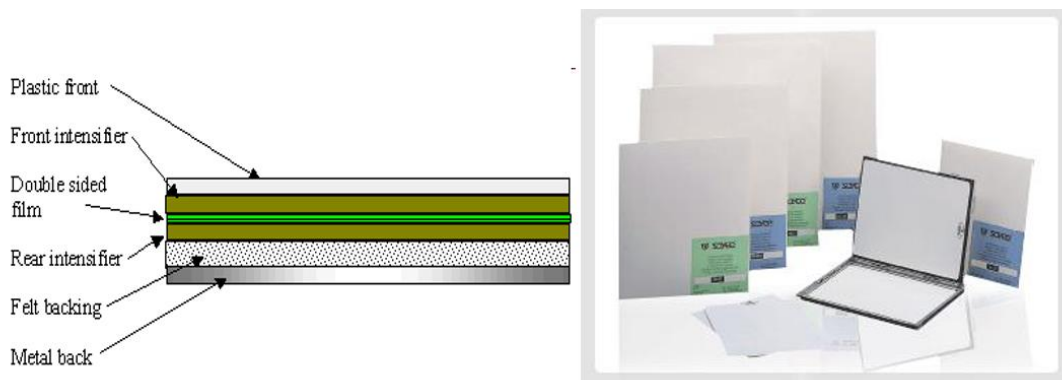
FIGURE 1-8: CROSS SECTION REPRESENTATION OF A FILM COVERED ON BOTH SIDES BY A FLUORESCENT SCREEN (RIGHT) EXAMPLE OF COMMERCIAL INTENSIFIER SCREEN BY SOYEE PRODUCT INC. SOURCE: [2]

Lately, in the 80's, the first digital detection system, Computed Radiography (CR), was introduced. To generate the image in these systems, first the phosphorus crystals layer is excited by the incident photons which implies a temporal energy storage; then the crystals are excited with a laser than unchains the liberation of the stored energy. This energy is gathered by an array of photomultipliers that turns it into an analogic electric signal. Finally, the analogic-digital conversion is performed. Figure 1-9 summarizes the process. The reading process has place outside of the clinical system, therefore the incorporation was easy, it was simply needed to change the detection panels and substitute the develop process by the reading one.
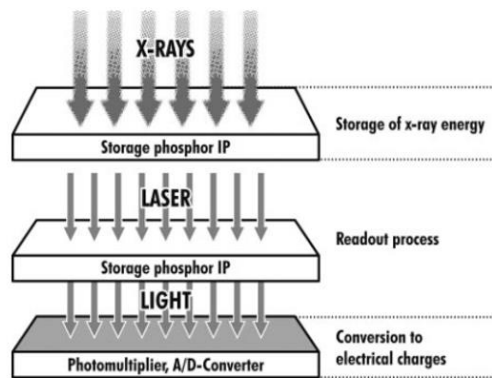
FIGURE 1-9: DIAGRAM OF A CR DIGITAL DETECTION SYSTEM COMPOSITION. SOURCE: [5]

Direct Radiography (DR) systems are developed, they turn the photon directly into an electric signal, suppressing the need of CR intermediate stages. DR systems are subdivided in direct DR and indirect DR depending on the conversion systems. In direct DR system photons are converted in electric signal in a single stage through a photoconductive material. Meanwhile in indirect DR, x ray photons are first transformed in visible light and then turned into electric charges by an array of photo-diodes. See figure 1-10
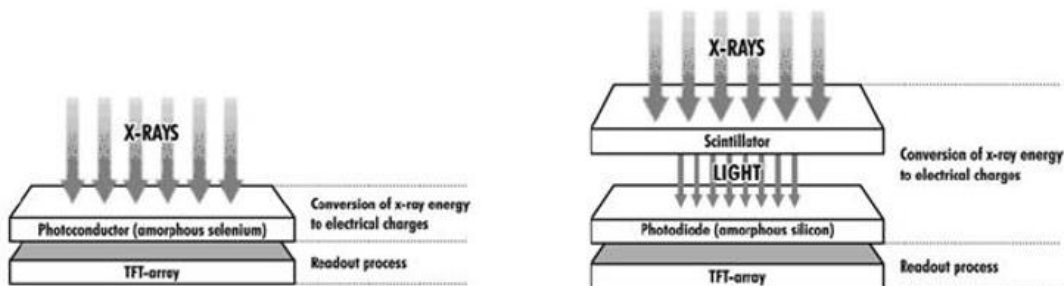
FIGURE 1-10: (LEFT) SHCEME OF A DIRECT CONVERSION DIGITAL DETECTION SYSTEM. (RIGHT) SCHEME OF AN INDERECT DIGITAL DETECTION SYSTEM. SOURCE: [5].

1.5 X-ray imaging

1.5.1 Projection

The data gathered in any of the systems previously described, is known as projections. Projections are a set of linear integrals of some property of the image. To understand the concept of projection we can see the example in figure 1-11. The square represents a two-dimensional image with different attenuation coefficients and the rays emulate a parallel beam geometry configuration. The projection for angle 0 is the sum of the attenuation coefficients through the different trajectories in that direction. Each projection represents the total attenuation traversed, while the t axis represents the distance from the x ray to the object center of coordinates. It is impossible to know the disposition of the attenuation values with only this information, but with another projection taken at 90 degrees it is possible to set a system of four linearly independent equations with four unknowns, and solve it. This example can be extended to real CT images, where there are much more unknowns and therefore much more projections are taken.
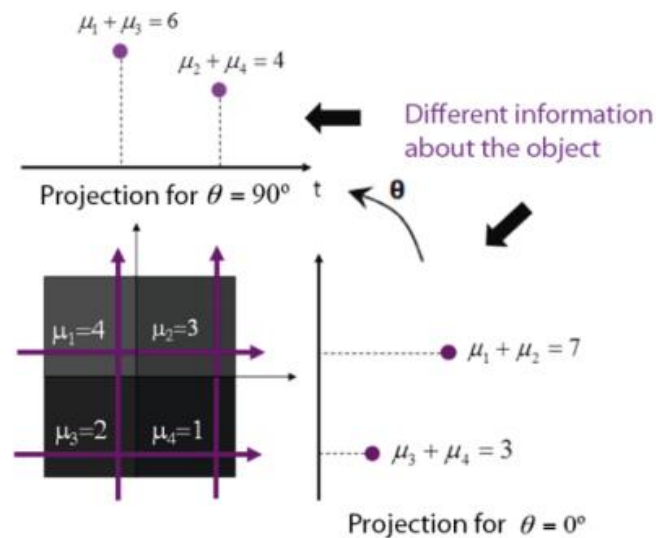
FIGURE 1-11: THE CONCEPT OF PROJECTION THROUGH AN EXAMPLE

The set of projections obtained for a single slice of the volume at different angles, are often organized in a sinogram as shown in figure 1-12
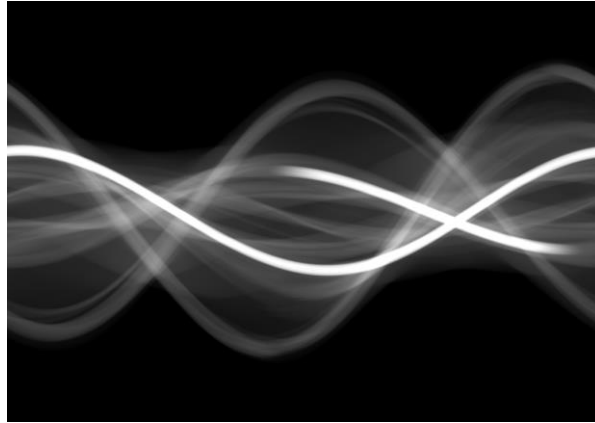
FIGURE 1-12: EXAMPLE OF A SINOGRAM.

1.5.2 Radiography

In radiography, a projective image of the radiated body is obtained. The photons that are not scattered nor absorbed by the sample or patient placed between the source and the photographic film are gathered in the detection. The amount of received photons in straight line from the source to a single spot in the film compared to the number of emitted photons depends on the attenuation coefficient of the material traversed and on the thickness of this material. Depending on the number of photons gathered, one gray level is assigned to the pixels of the image. Therefore, the x-ray image represents the tissue density, as we are measuring how many photons are stopped through the tissue.

The obtained image is projective, compressing the 3D volume of the patient into a 2D image which is not quantitative and makes harder medical interpretation. The whiter parts of the image correspond to the denser zones with higher photon absorption like bone; mid grey colors usually correspond to soft tissue with medium levels of photon absorption and darker areas correspond to very low densities such as air. Due to the slight density differences in soft tissue, best contrast is obtained in with bone (traumatology application) and with air (pulmonary imaging). Radiology is and has been the most used imaging technique in medicine; between 80 to 90 percent of the clinical images acquired belongs to this modality.

In conventional radiology, the x rays are gathered in a screen film detector, while in digital radiology the detector is electronic and generates a digital image. The main advantage in the latter case is the capability of post processing the acquire information. Numerous post processing techniques have been developed reducing the necessity of repeating imaging and radiating again the patient. Moreover it makes much easier data management, storage and

transmission. From digital radiology is developed computed tomography (CT) a technique that solves the tissue superposition problem.

1.5.3 X ray computed tomography system

Tomography is defined as: the use of X-rays to make three-dimensional images of flat sections of the body. The word etymology is greek, from *tomé:* cut and *grafos:* drawing.

Computed Tomography (CT) enables to separate different planes or slices of the radiated sample, which facilitates the visualization of a body section without the interference of surrounding regions. With this technique, it is possible to obtain small thickness cuts of the patient commonly in three directions: axial, sagittal and coronal. The process for obtaining images is separated in two main steps, projecting and reconstructing. First, several radiographies are taken at different angles from the same, and then the volume is mathematically reconstructed from the data in all the projections.

Different types of tomography systems have been developed since its inception:

First system where formed by a spot source and a small detector that had to be moved in small steps to get a full projection. Then, the source detector system would rotate and repeat the process for a different angle obtaining another projection. The trajectories described by the x rays were straight lines perpendicular to the projection plane (see Figure 1-13).
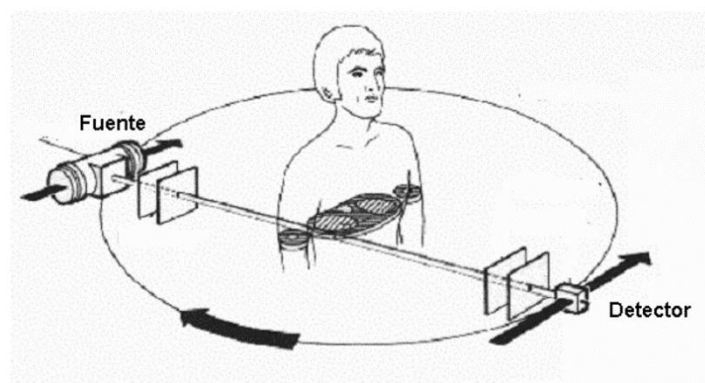
FIGURE 1-13: SCHEME OF THE FIRST CTS WITH PARALLEL RAY ACQUISITION

To take advantage of a larger part of radiated dose, not only the photons on trajectories perpendicular to the detector, the detector was enlarged becoming a row of small detectors. Besides the number of detector displacement needed were reduce. In this system, photon trajectories are nor parallel but diverge from a single point forming a fan beam geometry (see Figure 1-13).

Depending on the detector shape two configurations are possible (see Figure 1-14):

-Equidistant rays when the detector is a straight line

-Equiangular rays when the detector is arc shaped
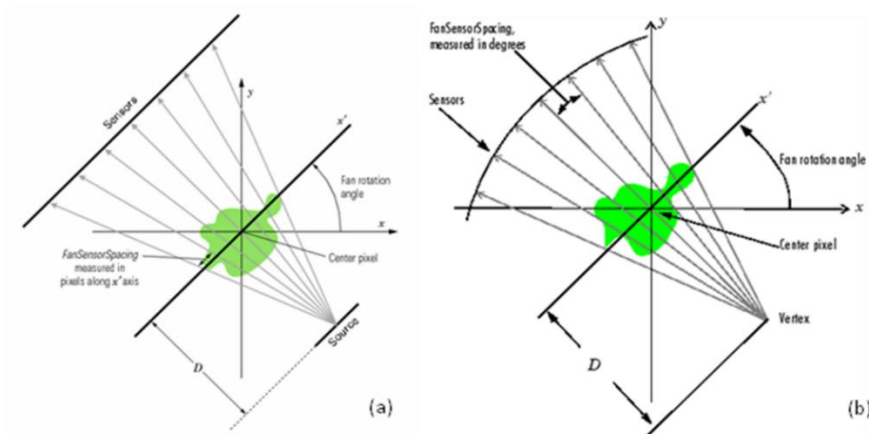
FIGURE 1-14: SECOND CTS GENERATION, FAN BEAM: (A) EQUIDISTANT RAYS, (B) EQUIANGULAR RAYS.

To make the acquisition even quicker the fan beam idea was expanded to the third dimension taking now advantage of the x rays emitted in all the directions, the detector became a plane This system geometry is known as cone beam geometry and is shown in figure 1-15.
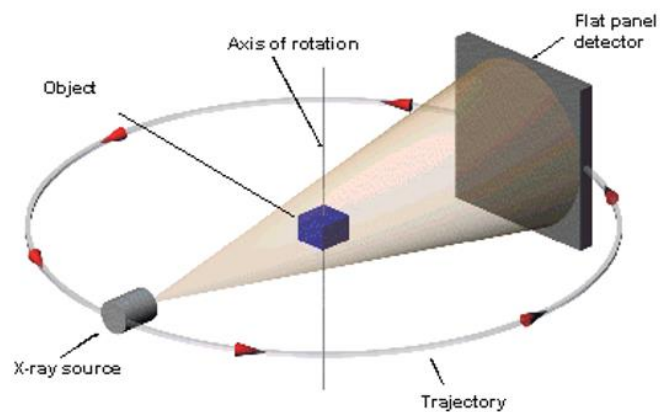
FIGURE 1-15: SKETCH OF CONE BEAM GEOMETRY CT ACQUISITION.

Finally, to speed up the acquisition, fan beam and cone beam concepts were extended to helicoidal acquisition. In this case, the patient is moved longitudinally as the source – detector systems rotates. Therefore, the x ray source describe an helicoidal trajectory. (see figure 1-16)
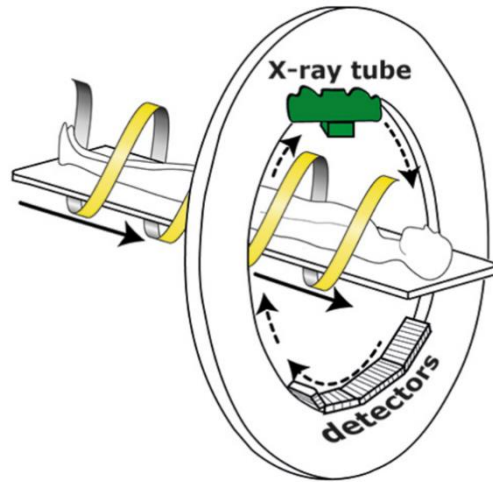
FIGURE 1-16: SKETCH OF AN HELICOIDAL CT ACQUISITION. SOURCE: [7]

1.5.4 Reconstruction methods

Image reconstruction in CT are mathematical processes that starting from x ray projection data acquired for different angles, generate an image. The quality of the image will be dependent on the reconstruction method, the better the reconstruction the lower the needed radiated dose. Reconstruction methods are classified in two major groups, analytical reconstruction and iterative reconstruction.

1.5.4.1 Analytical reconstruction methods

The analytical approach to image reconstruction is based on the discretization of an idealized mathematical model in the continuous space, assuming that the projections are line integrals of the volume to reconstruct.

The projections are assumed to be line integrals of the volume to reconstruct. The following equation describes this approach for parallel x rays (figure 1-17).

$$P_\theta(t) = \int_{(\theta,t)} f(x,y)ds = \int_{-\infty}^{\infty} f(x,y)\delta(x \cdot \cos\theta + y \cdot sen\theta - t)dxdy$$

$$t = x \cdot \cos\theta + y \cdot sen\theta$$

$$t = x \cdot \cos\theta_0 + y \cdot sen\theta_0$$
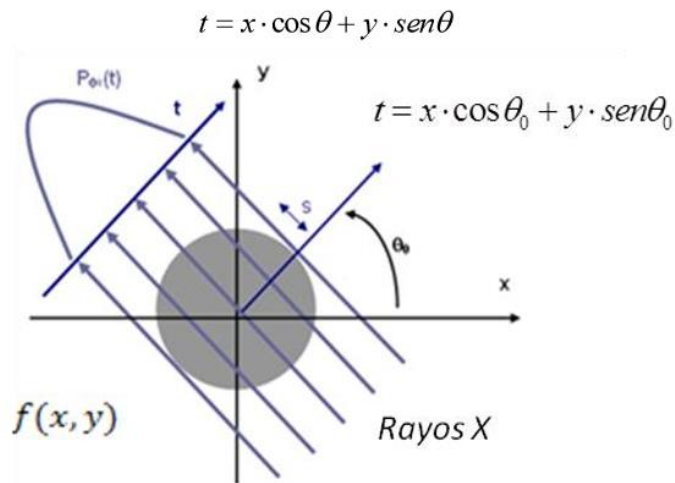
FIGURE 1-17: SKETCH OF PROJECTION. LINES REPRESENT PARALLEL RAYS THAT GO THROUGH THE OBJECT F(X,Y) FOR PROJECTION ANGLE ⵔO AND INTEGRALS ALONG EACH LINE REPRESENT THE PROJECTION VALUE FOR THIS ANGLE, PO(T)

Function $P_\theta(t)$ is the Radon transform of function $f(x,y)$. In two dimensions, the radon transform is the integral transform consisting on the integral of a function along straight lines. A projection is the combination of several line integrals. The central slices theorem states that "Fourier transform of a parallel projection of a f(x,y) distribution for a Ө angle, is equal to the values of the 2D Fourier transform of a distribution in the line passing through the origin and forming the same angle with u axis". This is used the fundamental relationship between the object and its projections for Radon Transform inversion. Figure 1-18 illustrate the central slice theorem.
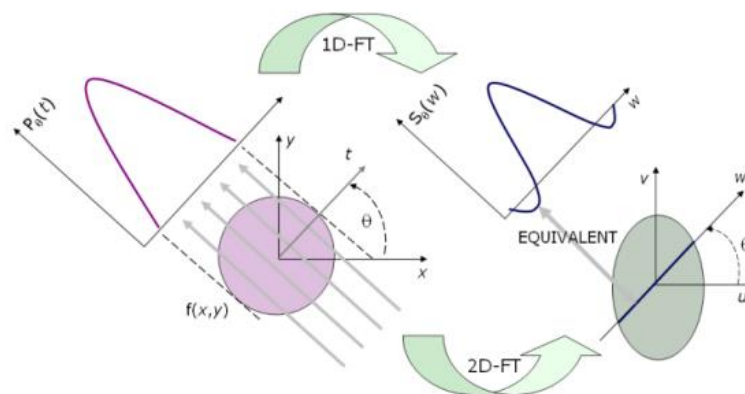
FIGURE 1-18: CENTRAL SLICE THEOREM. SOURCE: [8]

FILTERED BACKPROJECTION

Filtered Backprojection (FBP) is the most commonly used algorithm for CT reconstruction. This method reconstructs a two-dimensional function, a volume slice, from the one dimensional

projections of that slice at multiple angles. The projections are filtered before being backprojected.

To easily understand backprojection, the example in figure 1-19, shows the basics of the process. In this case with only to projections at 0 and 90 degrees. The backprojected image for 0 degrees is calculated repeating the values of the projection in each column. Then the backprojected image for 0º and 90º is obtained adding the 90º backprojected image to the 0º one.
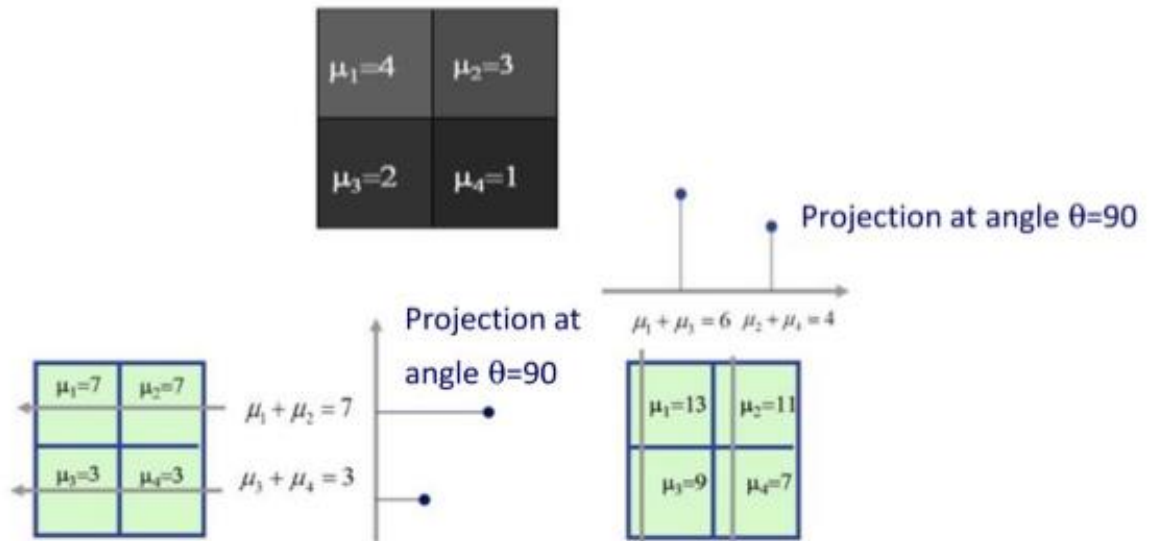
FIGURE 1-19: BASIC EXAMPLE ILLUSTRATING BACKPROJECTION CONCEPT.

However, in real applications, a larger number of projections is needed. Usually the one-dimensional projections at different angles for a same slice of the volume are arranged in sonograms, a two dimensional image, were each row is one of the projections. The number of rows will therefore correspond to the number of angles and projections.

Figure 1-20 shows that direct backprojection produces a very blurred image. The low frequency component of the image are dominant, therefore, before backprojecting the projections need to be filtered in order to enhance the high frequency components while keeping the low frequencies and obtaining a much better image. The sinogram is filtered in the Fourier domain using a ramp filter.
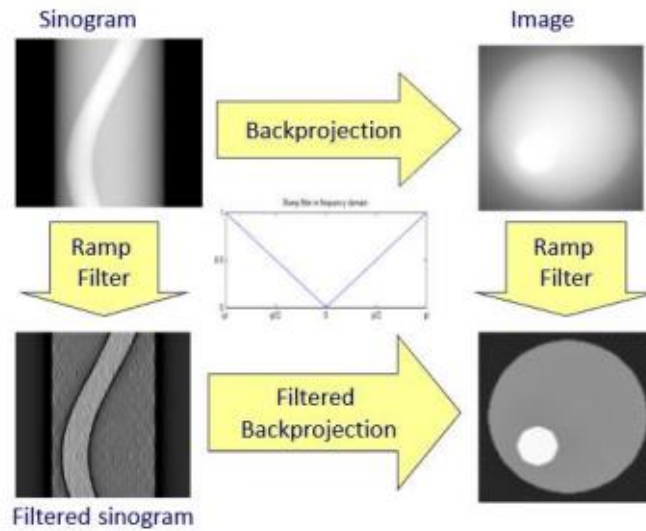
FIGURE 1-20: SCHEME OF THE DIFFERENT STEPS IN FBP AND FILTER EFFECTS

FDK RECONSTRUCTION

Many scanners utilize cone beam geometry with a detector displaced in circular path. In these systems reconstruction is done with the proposed method by by Feldkamp, Davis and Kress.

In this method, a third coordinate is added to the FBP reconstruction, enabling all rays to be considered from the proper coordinate system transformation. Besides, the object coordinates system and the real one are matched, in order to make the implementation more efficient. See figure 1-21
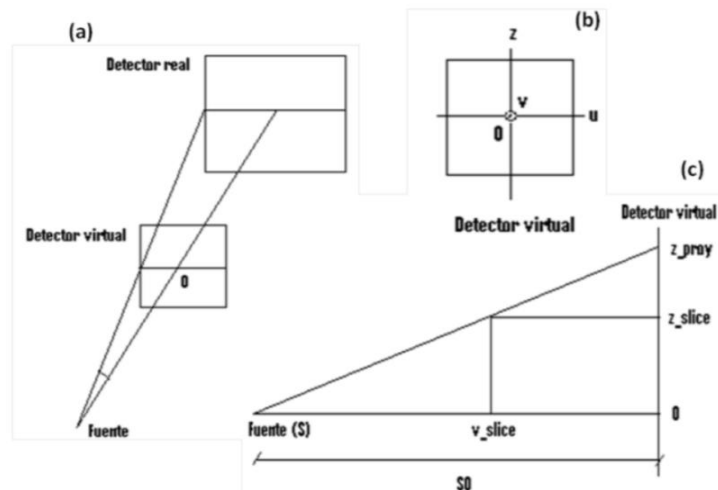
FIGURE 1-21: (A) PERSPECTIVE VIEW, (B) FRONT VIEW AND (C) LATERAL VIEW OF CONE BEAM GEOMETRY. FOR RECONSTRUCTION, REAL DETECTOR COORDINATE SYSTEM WILL BE MATCHED WITH VIRTUAL DETECTOR COORDINATE SYSTEM.

15

The information obtained in the projections of cone beam with circular trajectory belongs to several planes. Using FDK method, the sufficiency condition (tuy's condition) needed for reconstruction in cone beam geometry is softened. Although the Radon space is not complete, the whole volume can be reconstructed slice by slice.

1.6 CT artifacts

In imaging, the systematic difference between the reconstructed image and the real attenuation coefficients of the radiated sample is referred as *artifact*. CT images odds to have artifacts are higher than radiography images, as they are obtained from a much larger number of data and after reconstruction processing of these data. The artifacts in TAC can be divided in 4 categories following Barret et al 2004:

1. Caused by physical phenomena resulting from the image acquisition.
2. Caused by the patient issued from his movement or the presence of metallic materials in his body.
3. Caused by hardware imperfections, as misalignments in the detector.
4. Caused by software, as the reconstruction method.

1.6.1 Physical origin

1.6.1.1 Beam Hardening

Beam hardening is the process by which the mean energy of the x-ray beam is increased while traversing a material due to low energy photons are more likely to be absorbed. There is two factors involved in beam hardening; the dependence of the attenuation coefficient on the energy and the polychromatic nature of the X-ray. Therefore, x rays traversing different paths across the sample will emerge with different spectra resulting in inconsistent measures that will generate artifacts when reconstructing. Two types of artifacts can result from the beam hardening effect: *cupping,* in homogenous objects, and dark lines or streaks between dense objects in heterogeneous volumes. These effects are illustrated in figure 1-22.
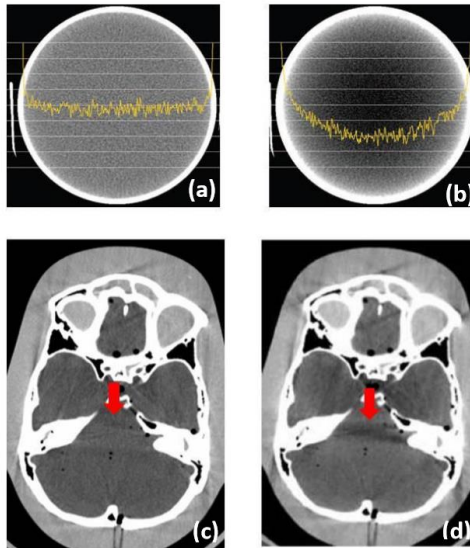
FIGURE 1-22: (A) AXIAL CUT OF THE CT IMAGE OF AN HOMOGENOUS CYLINDER WITHOUT BEAM HARDENING, WHERE THE YELLOW LINE REPRESENTS THE CENTRAL PROFILE, (B) SAME CUT BUT NON-HOMOGENOUS DUE TO BEAM HARDENING, THE CHARACTERISTIC SHAPE OF CUPPING CAN BE OBSERVED IN THE PROFILE, (C) AXIAL CUT OF CT IMAGE OF A HEAD WITHOUT BEAM HARDENING AND (D) SAME CUT WITH THE DARK BAND ARTIFACT DUE TO BEAM HARDENING (POINTED BY THE RED ARROW). SOURCE: [9]

1.6.1.2 Photon starvation

Photon starvation occurs when the number of photons reaching the detector is insufficient. When dense areas are traversed, a very large part of the photons are absorbed and not enough reach the detector, thus the signal received is too low while the noise is very high (low signal to noise ratio). In the reconstructed image artifacts will appear, such as the white lines in figure 1-23

FIGURE 1-23: CORONAL CUT (LEFT) AND AXIAL CUT (RIGHT) OF A CLINICAL CT IMAGE WITH PHOTON STARVATION ARTIFACT. SOURCE: [9]

1.6.2 Patient origin

1.6.2.1 Metallic artifacts

The presence of metallic objects in the field of view will introduce artifacts that diminish the image quality, as shown in figure 1-24. This is due to the high attenuation coefficients of the metal objects that impede detection of photons coming from this direction.

Sometimes those artifacts can be avoided by retrieving any metallic object from the patient, however, many times this may not be possible. For instance, when dealing with implants (hip, dental …) or peacemakers, post-processing techniques have to be used in order to correct or reduce the artifact.
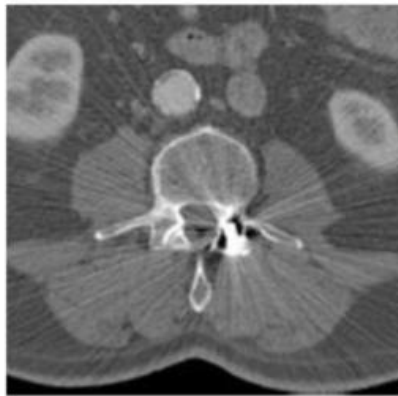
FIGURE 1-24 CT IMAGE SHOWING METALLIC ARTIFACT. SOURCE: [9]

1.6.2.2 Patient movement

Patient movements might lead to inconsistent projections which provokes artifact in reconstructed images as shown in figure 1-25. Besides, involuntary movements as respiration can cause strong artifacts in the diaphragm area. When possible, the patient is requested to inspire as much as possible and keep the air inside during the whole CT radiation process. However, when dealing with unconscious subjects this is not possible. When it comes to thorax or cardiac dynamic studies, the respiratory or cardiac signals can be measured. Based on them, projections can be taken only at a given time of the respiratory or cardiac cycle, ensuring consistent projections for reconstruction.
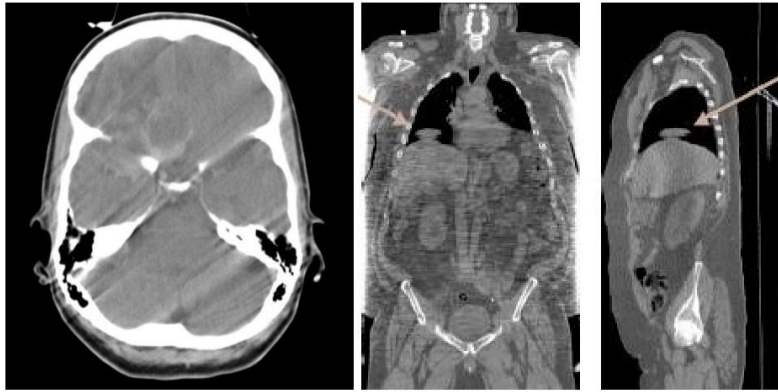
1.6.3 Scanner origin

1.6.3.1 Ring artifact

Reconstructions from CTs equipped with flat panel detectors and that describe circular trajectories are prone to have ring artifacts that difficult the quantitative analysis of the image as the example in FIGURE X clearly shows. Those artifacts are a consequence of detector pixels' difference in gain. This artifact can be reduced in post processing, after the reconstruction or at the projections and also by calibrating all the detectors. Figure 1-26
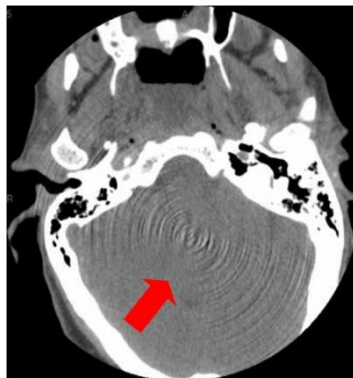
FIGURE 1-26: AXIAL CUT OF A BRAIN CT IMAGE WHERE THE RED ARROW POINTS RING ARTIFACTS. SOURCE: [9]

1.6.3.2 MECHANICALLY ORIGINATED ARTIFACTS

This kind of artifacts are originated by the small imperfections in the fabrication process, especially those in the positioning of the detector. The detector may present different geometric misalignments with respect to its ideal position in the CT as shown in figure 1-27.
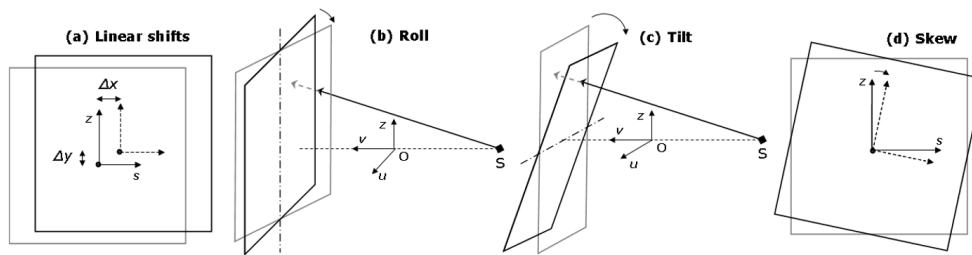
FIGURE 1-27: DETECTOR MISALIGNMENTS [10]

The different artifacts, depending on the detectors misalignment are shown in figures 1-28 and 1-29.
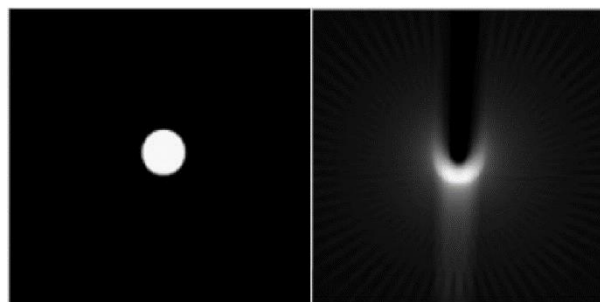
FIGURE 1-28: EXAMPLE OF (LEFT) RECONSTRUCTION WITHOUT MISALIGNMENT AND (RIGHT) RECONSTRUCTION WITH HORIZONTAL DISPLACEMENT OF THE DETECTOR [11]

To correct these artifacts the device must be calibrated to obtain the necessary parameters for compensation during the reconstruction stage.
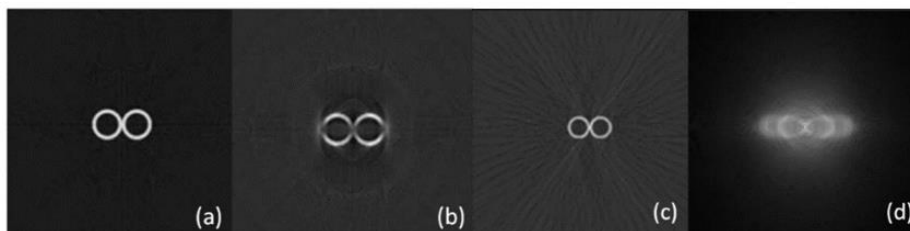
FIGURE 1-29: RECONSTRUCTED IMAGE WITHOUT MISALIGNMENT (A), WHEN THE DETECTOR IS INCLINED N/10º AROUND ITS CENTRAL AXIS (B), WHEN THE DETECTOR TURNS N/4º AROUND ITS VERTICAL AXIS (C), WHEN THE DETECTOR ROTATES N/7º IN THE SAME PLANE (D). SOURCE: [11]

1.6.4 Artifacts in reconstruction

1.6.4.1 Number of samples and number of projections.

There are two important factors in acquisition, number of samples in each projection and number of projections. A low quantity of any of those variables may cause artifacts when reconstructing. A high number of projections (K) with a low number of samples causes artifacts

in the form of bands due to aliasing. The projection is sampled at a lower number than Nyquist frequency and some information is lost. On the other hand, a low number of projections will cause artifacts too, due to scarcity of acquired data at different angles (see figure 1.30).
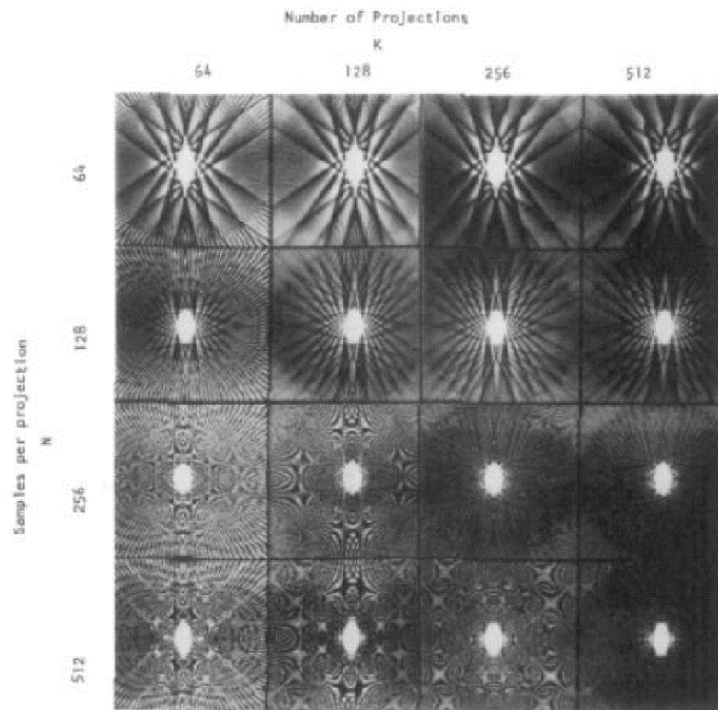
FIGURE 1-30: DIFFERENT RECONSTRUCTIONS OF AN ELLIPSE FOR DIFFERENT NUMBER OF PROJECTIONS (K) AND NUMBER OF RAYS IN EACH PROJECTIONS (N). SOURCE: [12]

1.6.4.2 Truncated projections

When the subject is larger than the FOV (field of view) of the CT scanner, the acquired projections will not match the complete projections of the subject but will be truncated to the size of the FOV. If it is reconstructed with an analytical method, such as FBP, the filtration stage will cause problems. The fast Fourier transform of the projections will have very high frequency components due to the projections' truncation. When multiplied in the frequency domain by a ramp filter, those high frequencies are enhanced, whereas they should not even appear. Figure 1-31 shows a reconstructed image with truncation artifact. A possible solution is to reconstruct a smaller region of interest instead of the whole volume.

FIGURE 1-31: CT IMAGE WITH ARTIFACT (WHITE BAND) BECAUSE THE PATIENT DIAMETER IS LARGER THAN THE FIELD OF VIEW.

2.CONTEXT, MOTIVATION AND OBJECTIVES

2.1 Motivation

Since the early 1970s, microcomputed tomography (micro-CT) systems have become an important imaging tool in preclinical and basic research due to the employ of animal models to study different conditions in humans (Schambach 2009). The largest number of human diseases have been developed on rodents due to its genetic similarity to humans, as well as good knowledge of these models and low cost (Lewis et al 2002). CT systems are the preferred technique to obtain high resolution, three-dimensional, anatomical images. Besides, the noninvasive nature of this technique brings the possibility to perform longitudinal image-based quantitative measurements in animal models eliminating the need for the animal to be slaughtered.

The work included in this thesis is framed on a research line with the objective of developing new systems of data acquisition, processing and reconstruction of multimodal images for applications in biomedical research. This line of research is carried out by the Biomedical Imaging and Instrumentation group from the This line of research is carried out by the Biomedical Imaging and Instrumentation group (BiiG) from the Universidad Carlos III de Madrid working jointly with the Gregorio Marañón Hospital through its Instituto de Investigación Sanitaria. Within this research line, the high-resolution multimodality scanner for small animal ARGUS PET/CT has been developed and it is currently being commercialized worldwide by the Sociedad Española de Electromedicina y Calidad S.A.

This system is used in different preclinical research lines in the group. One of these research lines focuses on the use of brain stimulation as Parkinson disease treatment. Rats have stainless electrodes implanted and fixed with screws in the lateral hypothalamus, through estereotaxia surgery. The CT subsystem of ARGUS is used then to corroborate the surgery was correct and the position of the electrodes is the right one.

The presence of metallic objects creates severe streak artifacts in CT images affecting image quality and hindering the correct representation of anatomy. The reason why is that metals have

a very high attenuation coefficient to rays compared to the human body, which creates a barrier to the transmitted x-ray beam during CT examination, resulting in a lack of data at the projections. The beam hardening correction method, already integrated in the ARGUS system results insufficient for the correction of the artifacts derived from the presence of metals. Motivated by this context, the objective of this thesis is to implement an algorithm for metal artifact correction to be included in ARGUS.

2.2 Regulatory framework and socio-economic environment

For many years, animals were not considered sentient beings and the main driving reason to limit their use in investigation was to reduce expenses. However, in the last decades, the consciousness that animals are sentient being and the respect for their lives has grown in society. This confronts with the increasingly importance of animal models for investigation and development in medical fields resulting in a complex bio-ethical conflict opposing the ambition for new medical equipment and treatments to the use of animals as mere means to an end. Today, investigation with living beings is reviewed and authorized by ethic comities. Besides, when requesting founds for these investigations or before publishing results in scientific journals, the ethics features of the methods used are examined.

In 1959 the three 'Rs' were introduced by, British zoologist W. M. S. Russell. The 3Rs are three principles for more ethical use of animals in testing [30-31]:

- **Replacement**: methods which avoid or replace the use of animals in research
- **Reduction**: use of methods that enable researchers to obtain comparable levels of information from fewer animals, or to obtain more information from the same number of animals.
- **Refinement**: use of methods that alleviate or minimize potential pain, suffering or distress, and enhance animal welfare for the animals used.

The scope of this principles is not only to encourage the alternatives to animal use but also to improve animal welfare and scientific quality where the use of animals cannot be avoided. Currently these principles are endorsed in many countries legislation, including Spain, and in international legislations.

When it comes to the application of CT imaging in investigation with animals we find a duplicity in the advantages it brings, not only broadening the techniques and resource for a greater progress in medicine but also enabling a stricter compliance of the 3 'Rs'.

2.3 Bibliography review

In the last decade, many approaches have been proposed to reduce these artifacts. Some of them try to approach the problem at the data acquisition stage. For instance, Meng Wu in 2017 proposed completing the missing kilovoltage projection data using selectively acquired megavoltage data [13]. The same year, Ballhausen et al proposed post-processing sets of tilted CT volumes as a method for metal artifact reduction [14]. This method requires a more laborious acquisition process and often entail a higher dose to the subject.

Nonetheless the most frequent techniques are based on the post-processing of the standard acquired data in a study. The majority of this proposed methods can be classified in two groups: iterative methods and inpainting methods.

An iterative method is a mathematical procedure that generates a sequence of improving approximate solutions for a class of problems, in which the n-th approximation is derived from the previous ones. Whether it is in the projection or data spaces, iterative algorithms work in a feedback mode. The major drawback of these methods are the extremely high computational costs that often require an implementation in specialized processor unit and that the manufacturers of CT imaging devices are often reluctant to provide the original raw projection data. Besides they still need to be combined with sinogram inpainting correction when dealing with rather severe metal artifacts.

Inpainting refers to substituting some parts of an image. In inpainting methods [17-25] the region of the projection or sinogram corresponding to trajectories with metal structures is identify by segmentation and substituted by interpolation. Some of these methods add other steps to improve the correction accuracy. These methods can be implemented without the original raw projection data and are less computationally expensive.

In 1987 Kalender [22] proposed an inpainting sinogram algorithm for MAR. Although this method reduced metallic artifacts, new artifacts were introduced and high frequencies were lost near the implant. Meyer in 2009 overcame this problem, normalizing the sinogram before applying the method, and denormalizing after. This normalized artifact reduction method (NMAR) was improved afterwards. In 2012 Meyer applied frequency split technique (FSMAR) to the NMAR corrected image, obtaining an even better quality. The method proposed by Meyer has had great success, being cited in many publications [14-17].

Moreover, the iterative MAR (iMAR) technique developed by Siemens (Siemens Sector Healthcare, Forchheim, Germany) in 2015 utilize an iterative implementation of inpainting

methods NMAR and FSMAR proposed by Meyer [ref]. Bär et al. [21], evaluates the iMAR technique and conclude that geometry and CT number accuracy can be re-established with iMAR as if there were no metal artifacts, independent of the density of the introduced metal substitute.

Due to the mentioned drawbacks, we dismissed iterative methods. Among the inpainting ones, we decided to base our MAR algorithm in the NMAR and FSMAR ones proposed by Meyer because of their good reviews and reception.

2.4 Objectives

The general objective of this thesis is to develop a metal artifact reduction (MAR) method for the ARGUS system. This general objective can be divided in the following tasks:

1. Software implementation of MAR algorithm
2. Evaluation of MAR algorithm on simulated data. The simulations are performed using FUX-Sim, a software tool previously developed by the group
3. Evaluation of MAR algorithm on real data, using two rodent studies acquired with the ARGUS system.

2.5 Structure of the manuscript

The manuscript is comprised of the following chapters:

- **Chapter 1:** Introduction. The physical fundamentals for x ray imaging are explained, including x ray generation, interaction with matter and detection. Then the mechanisms of CT and different reconstruction techniques are presented. Finally, the origin of the different artifacts that occur in CT imaging are exposed.
- **Chapter 2:** Motivation and objectives. This chapter portrays the contextual framework of the project, highlighting the importance of CT imaging in preclinical research and providing the context and reasons to choose the MAR method implemented in this project.
- **Chapter 3:** Methods. In this chapter, the implementation of the MAR method and its evaluations are presented. First of all, a description of the CT system under study is provided, followed by the explanation of FUX-Sim, a software simulation tool crucial for thins project. Then the steps followed for implementing the correction algorithm are detailed. In the last part, the methods for evaluation are explained.
- **Chapter 4** Results. This chapters describes the results of the evaluation realized for the implemented MAR method.

- **Chapter 5:** Conclusions and future work
- **Chapter 6:** Project management.

3. METHODS

The process of implementing the Metal Artifact Reduction method (MAR) has been carried out in several steps and implemented in MATLAB (The MathWorks Inc., Natick, MA, USA). This required the use of existing or newly developed software tools that are described in this chapter.

In the first section, we describe the system under study. In the second an in-house developed software tool for geometrical X-ray simulation and reconstruction, FUX-sim. The third section explains the implementation of the method for reducing metal artifacts carried out through this project. Finally, we describe the workflow for evaluating the algorithm proposed, outlining the tools developed and the metrics applied for it.

3.1 System under study

The CT subsystem of the Argus PET/CT is a third generation multimodal micro-CT developed by BiiG. It is integrated with a nuclear imaging systems, PET and SPECT, and optical imaging. A microfocus X-ray source and a flat panel with CMOS technology and a microcolumnar CsI scintillator plate are the main component of the system's hardware. Both the source and the detector are located on the gantry able to rotate, enabling the acquisition of projections at different angles around the bed, the platform between them where the subject is located. Continuous rotation of the gantry in one direction without cable wrap around is possible due to the use of slip rings. The movement of the bed and the rotation are managed from a control PC (general purpose machine AMD Opteron 242 1.6 GHz, 1 MB of RAM, Linux OS 2.4.21).

The components of the x ray tube (Apogee 5000 series, Oxford instruments) are: A tungsten anode and beryllium window of 126 μm. The maximum power and voltages it achieves are 50 W and 50 keV respectively.

The micro CT system operates with cone beam geometry, represented in figure 3-1

$$D_{SO} = 220 \; mm \qquad D_{DO} = 132 \; mm$$
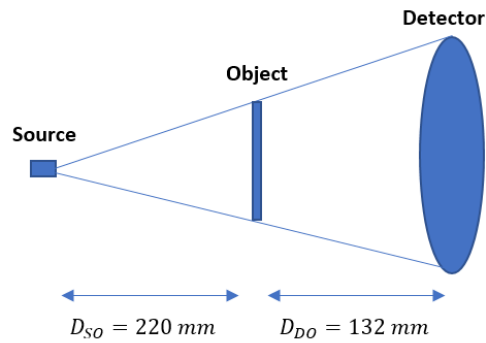
FIGURE 3-1: SCHEME OF THE MICRO-CT SYSTEM GEOMETRY

Besides, the system is fitted with a multimodality workstation MMWKS (Pascau *et al* 2006)[26], and the multi-bed reconstruction software Mangoose® (Abella *et al* 2011)[27].

For every study, the obtain projections are save in files with extension '.CTF'. The study metadata (number of projections, projection size, span angle, pixel size, current and voltage during acquisition, etc) is in a '.ACT' file. The number of '.CTF' files generated per acquisition will depend on the number of projections and the number of pixels per projection.

When reconstructing the obtained volume is in a file with extension '.IMG'. The reconstruction meta data (number and size of projection, pixel and voxel sizes, voltage and amperage of the source, etc.) is in a file with extension '.HDR'.

3.2 Simulation tool: FUX-SIM

FUX-Sim is a simulation tool that mimics the behavior of x-ray systems [27]. This tool has been developed a by the BiiG group from UC3M in association with ARCOS from the same university, who were in charge of accelerating the code using parallel processing on Graphic Processing Units (GPUs)., who were in charge of accelerating the code thanks to parallel processing in Graphic Processing Units (GPUs). This software simulates a CT scanner and is also able to reconstruct volumes from CT images.

FUX-Sim allows us to:

- Project and reconstruct volumes operating with different modes (regular CT, tomosynthesis, planar x ray and wide FOV).
- Choose the system features
    - o Detector panel and source positions
    - o Detector panel and volume sizes

        o   Sizes of the pixels (in projection) and the voxels (in volume)

        o   Source voltage

        o   Scanner rotation

- Select different span and step angles.

- Manage different data types (signed short, unsigned short and float).

- Choose the data interpolation (ray/voxel-driven or distance-driven).

- Work with Regions Of Interest (ROI).

- Emulate real detector panels including their possible misalignments (vertical and horizontal shifts, rotations and inclinations).

- Simulate the system calibration.

FUX-Sim is based on cone-beam geometry both for CT and for planar X-ray images. Such systems are characterized by a single source of radiation and a flat-panel detector that rotates around the volume describing a complete or partial orbit (CT), that is fixed or that moves linearly in a table or a wall stand (planar X-ray images). See figure 3-2
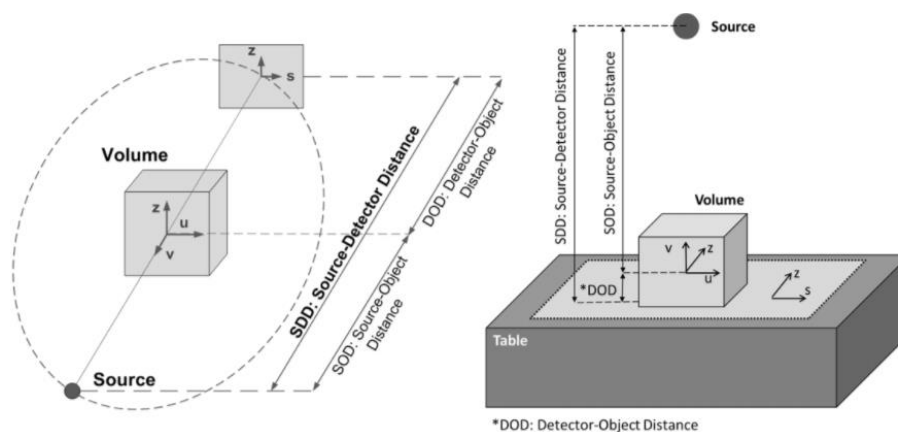
FIGURE 3-2: FUX-SIM GEOMETRY

The distance between source and detector is called Source-Detector Distance (SDD) and it can be separated into the Source-Object and the Detector-Object distances. Object refers to the volume we project or reconstruct. It is formed by uxvxz voxels and its resolution is selected by the user. The detector, on the other hand, is composed by sxz pixels of selectable sizes.

FUX-Sim has two types of simulation modes:

- **Projection:** we can acquire one (planar X-ray) or several (CT, wide FOV and tomosynthesis) projections of the volume.

- **Backprojection:** we spread back the values of the projections along each ray obtaining a blurred 3D image (low frequency). We can apply a ramp filter to attenuate the low frequencies and accentuate the higher ones.

FUX-Sim has several configurations modes. For the work presented in this thesis cone beam CT configuration is used.

3.3 Implementation of the Metal Artifact Reduction algorithm

The implemented MAR method is based on the one proposed by Meyer in 2009 [23] and the updating published in 2012 [24]. Its underlying principle is to consider sinogram values as unreliable when those correspond to rays that have traversed any metal. These values are therefore replaced by interpolation. However, a major drawback of interpolation is the loss of edge information in the metal trace and the observation of added streaks in the image. To offset these disadvantages, a normalization step is introduced. Before interpolating the image, it is normalized by a *prior image* and once interpolated, it is denormalized.

Correcting with inpainting methods such as this one tends to eliminate high frequencies, and image quality near the implant is very poor. However, in uncorrected images the outlines of anatomical structures, high frequencies, are often conserved even when covered by artifact streaks, they have wrong CT values but can be detected. To exploit this, we perform a frequency split correction at the end, a technique that combines parts of the high frequencies of the uncorrected images with the low frequencies of the MAR corrected one, in order to obtain and even better correction.

The following sections contain a detailed explanation of the method, step by step. Figure 3-3 shows a flow diagram of the process.

FIGURE 3-3: DIAGRAMS OF THE STEPS IN MAR CORRECTION

First, the original volume, f^{orig} is reconstructed from the x ray projections obtained either from the simulator or the real CT system p^{orig}. Then this volume is segmented by thresholding; a convenient threshold is choose in order to put everything but the metal area to 0, leading to a metal volume, f^{metal}.
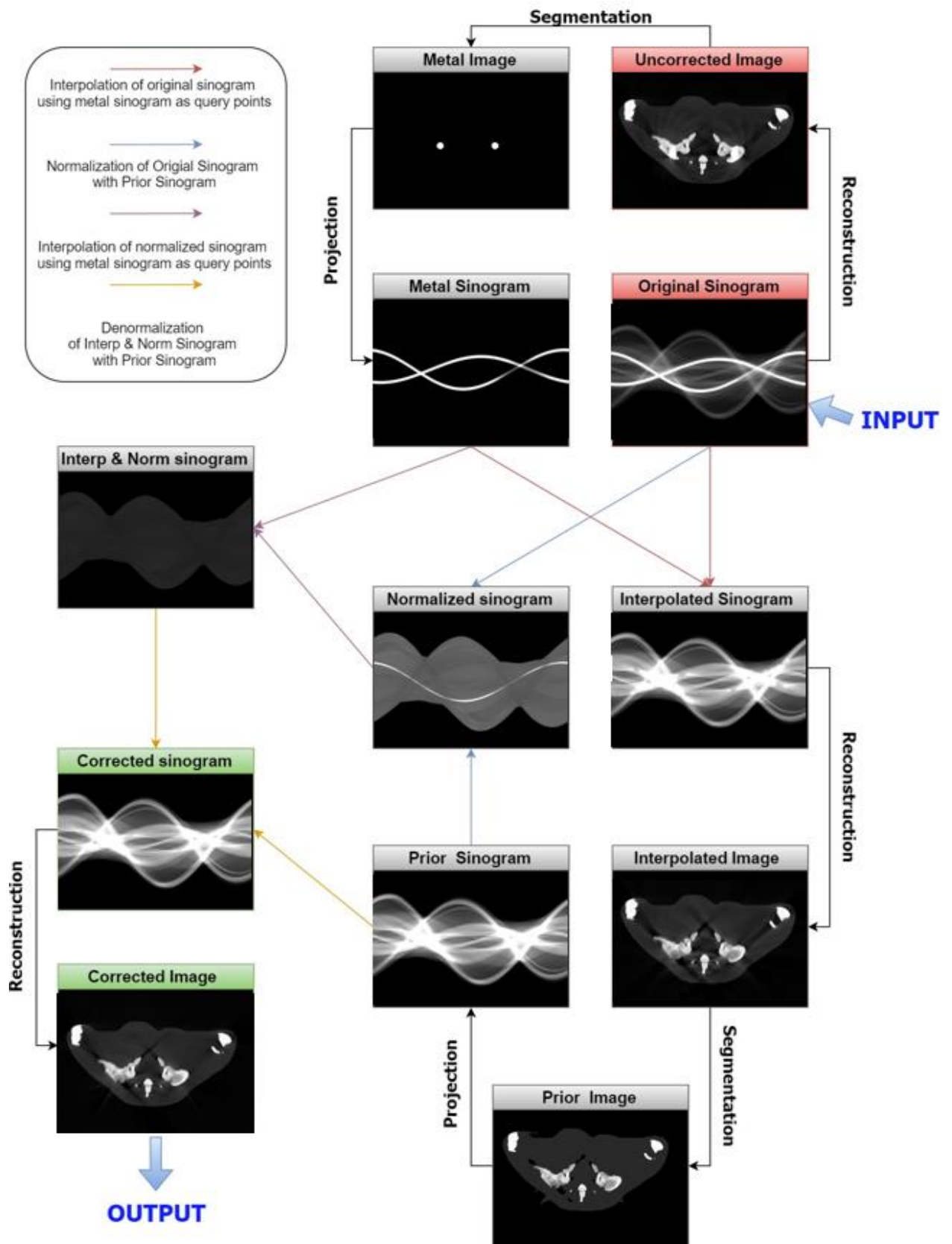
After that, f^{metal} is projected with fux-sim, obtaining a sinogram where every non zero point correspond to a trajectory with any metal in it. These points are used as query points in order to interpolate the original projections p^{orig}. Several methods can be used for interpolating however, we apply linear interpolation. Now f^{interp} is reconstructed from the interpolated sinograms.

Then a prior image, f^{prior}, is obtained from thresholding f^{interp}. Background, soft tissue and bone are segmented. For the background a very small value close to 0 is set to every pixel, as any 0 value will impede further division by f^{prior}. When it comes to soft tissue, the mean value is computed and assigned to every pixel. Bone is left with its current values.

In reference [x] the method works using binary images to normalize, however metal implants are likely to be located near bone tissue, and often the region surrounding the implant is intended to be studied. Therefore, to obtain better results a prior image needs to be used.

The more homogenous the data, the less problematic the interpolation. Therefore it is interesting to transform the sinogram and make it as flat as possible. It has been stated that the projection or Radon transform is depending on the attenuation coefficients of the material traversed but also on the length of the path. When projecting an object made of a single material, if we divide each projection value by the traversed length, the sinogram would have the same attenuation value everywhere. To mimic this concept for three materials, p^{orig} is divided by the projections of f^{prior}, that has 0 value for background and an average for soft tissue, and we achieve a normalized sinogram, p^{norm}.

Now we interpolate y^{norm}, and then we denormalize it multiplying by p^{prior}, obtaining the corrected projection p^{MAR}. The only thing missing is to reconstruct these projections in order to generate f^{MAR}.

To put the whole method in a nutshell, let M be the interpolation operation that uses the sinogram of f^{metal} as query point then:

$$p^{MAR} = p^{prior} \cdot Mp^{norm} = f^{prior} \cdot M \frac{p^{orig}}{p^{prior}}$$

Now we are going to separate the high frequency and the low frequency components of f^{orig} and f^{MAR}.

Both f^{orig} and f^{MAR} are low pass filtered and denoted f^{origlo} and f^{MARlo}. This is done by a two-dimensional convolution with a Gaussian. Meanwhile the high frequency versions are called f^{orighi} and f^{MARhi}. The high frequency images are obtained subtracting the low pass filtered image to the original one. f^{orighi} contains the edges and thin anatomical structures. On the other hand, f^{MARhi} contains less artifact but it also contains less edges close to the metal implant. It is then interesting to combine these both images, applying a higher weight to pixels surrounding the implant in f^{orighi} and to pixels far from the implant in f^{MARhi}. For that, a weight image, W, is generated using f^{metal} and dividing by its maximum. For creating W, the metal image is binarize, then it is smooth with a strong low-pass filter and normalize to a maximum value of 1. The final f^{FSMAR} is obtained by:

$$f_{ij}^{FSMAR} = f_{ij}^{MARlo} + W_{ij} \cdot f_{ij}^{orighi} + \left(1 - W_{ij}\right) \cdot f_{ij}^{MARhi}$$

with $i = 1, \dots, I; j = 1, \dots, J$ and where I and J are the number of rows and columns respectively in an image.

3.4 Evaluation

We evaluated the effectiveness of our MAR algorithm on simulated data and on real data acquired in the ARGUS scanner. Apart from visual analysis of the corrected images evaluate the images using the root mean square error (RMSE) and intensity profiles in an ROI affected by metallic artifact. The first part of this section details how the simulation was done. Then, the real studies are presented. Finally, the figures of merit are explained.

3.3.1 Simulated data

The first evaluations of the method have been done using simulated data. This provides much more flexibility than real data since without the cost of performing a real CT we can test the method for implants of different sizes, shapes and metals.

In order to obtain simulated data with metal artifact a digital mouse phantom, called *digimouse,* was used [29]. This phantom is a three-dimensional matrix representing the density values of the soft tissues and bone of a mouse. The original *digimouse* volume has been adapted for our

simulation in order to create a phantom containing the abdomen and the hips of the digital mouse, which lead to a final volume of 380x380x380 pixels. Figure 3-4 represents three orthogonal views of the resulting digimouse.
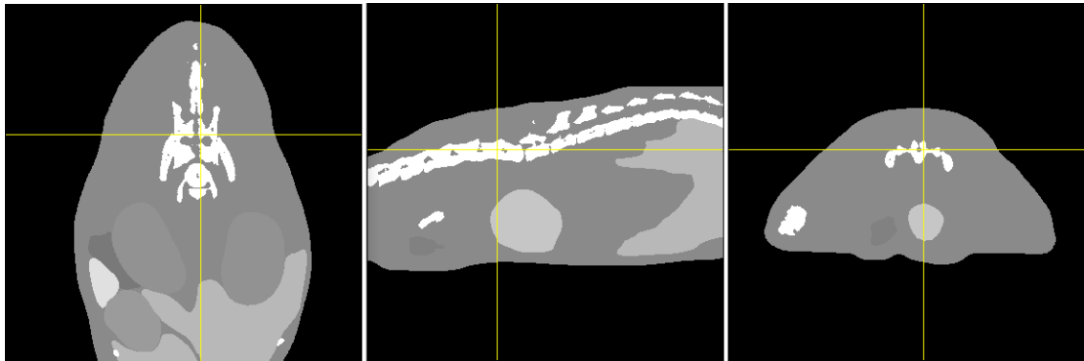
FIGURE **3-4:** THREE ORTGHOGONAL VIEWS OF DIGIMOUSE VOLUME

In order to simulate different situations involving different types and amount of metals, the digimouse volume was modified by introducing different regions with the corresponding metal densities. The locations were picked based on real studies locations for metal implants such as the hip or between to vertebras. In Figure 3.5 we can observe a transversal cut of digimouse with the simulated gold implant.
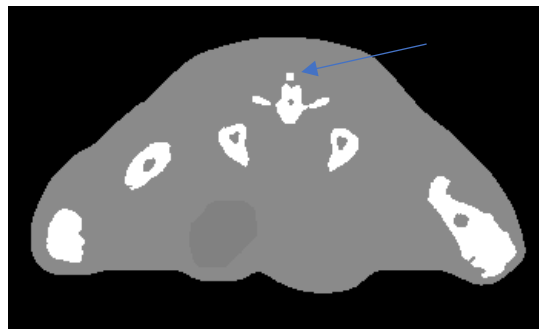
FIGURE **3-5:** DIGIMOUSE TRANSVERSAL CUR, THE ARROW POINTS OUT THE GOLD IMPLANT

Generating an X-ray image implies that a photon beam has to pass through a sample. The detector counts the received number of photons ($Nout$) after crossing the sample, and relates them with the emitted number of photons at the source (Nin) by Beer Lambert's law.

For monochromatic light, the equation is

$$N_{out} = N_{in}e^{-\int_L \mu \, dl}$$
(3.1)

When a polychromatic spectrum is used as the attenuation coefficient depends on the photon energy the equation becomes as follow:

$$N_{out} = N_{in}e^{-\int_L \Sigma_i \mu_i\ dl} \qquad (3.2)$$

We clear the equation to obtain the total attenuation which is the logarithm of the ratio between the emitted photons and the received ones.

$$\int_L \Sigma_i \mu_i\ dl = \ln(\frac{N_{in}}{N_{out}}) \qquad (3.3)$$

Where L is the length of the traversed material and $\mu(x)$ is the linear attenuation coefficient of the object. The linear attenuation coefficients describe the attenuation properties of a particular material. Those are dependent on two factors, the energy of the incident photon, and the density of the material. Therefore, the attenuation properties of water not only are different for different energies of x rays but also for will be different for ice, liquid water or steam. However, density dependency of μ is linear, the μ normalization by the density is called mass attenuation coefficient $\left(\frac{\mu}{\rho}\right)(MAC)$. Being the mass attenuation coefficients of ice, liquid water and steam, exactly the same.

$$N_{out} = N_{in}e^{-\int_L \Sigma_i mac_i \cdot \rho_i\ dl} \qquad (3.4)$$

The objective of the simulation is to obtain *Nout*. To obtain it, we implement a Matlab function that applies Beer's law for 3 tissues. The workflow of the function is the following:

First, the digimouse volume is segmented into three separate volumes, one for each tissue: soft tissue, bone and metal.

Next, we utilized FUX-Sim to get $\rho \cdot dl$. Our volumes contain the density information and are projected with FUX-Sim which is set to the desire projection parameters (number of projections, span angle, projections size…). The results are 3 stacks of projections, an example is shown in figure 3-6
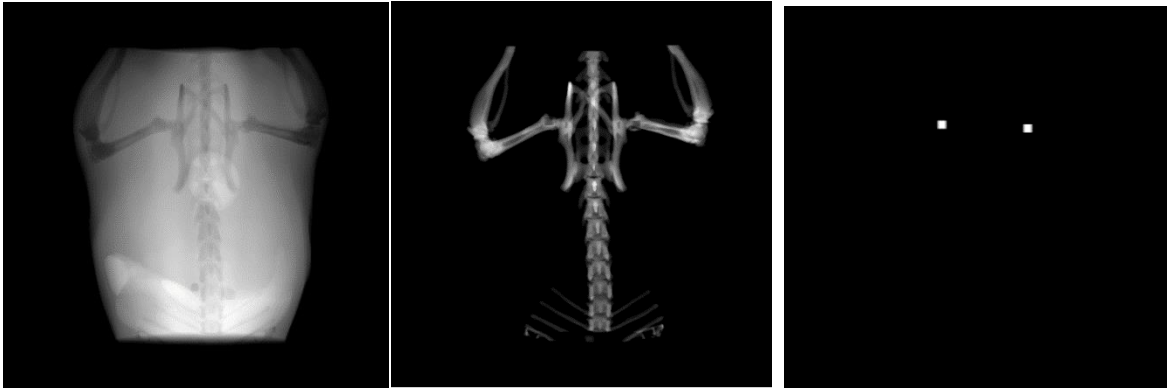
FIGURE 3.6: PROJECTION OF THE THREE SEGMENTED VOLUMES OF DIGIMOUSE (LEFT) SOFT TISSUE, (MID) BONE, (RIGHT) METAL

Secondly, we have to provide the mass attenuation coefficients for bone, soft tissue and metal, and the x ray spectra we want to simulate. We obtained the MACs from the National Institute of Standards and Technology (source C). The spectra used in our simulation is a 40KeV spectra, which imitates a scanner for small animal. We obtain N_{out} as in equation (3.4).

Finally, we obtain the attenuation image calculating the logarithm of N_{in} divided by N_{out} as states equation (3.3). Figure 3-7 shows the attenuated projections
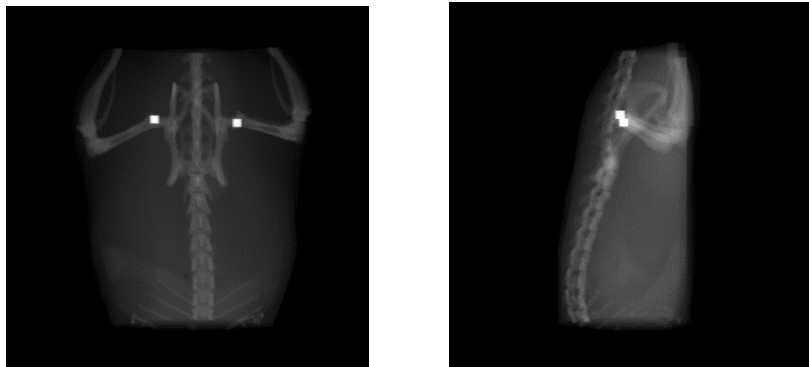
FIGURE 3-7: ATTENUATION IMAGE FOR TO DIFFERENT ANGLE PROJECTIONS OF THE TWO HIP IMPLANT SIMULATION EXAMPLE.

We have implemented three simulations: the first one is a single titanium hip implant, the second one is a double titanium hip implant and the third one is an inter-vertebral gold implant. The projections of these artifacts are shown in figure 3-8. We chose these materials because they are often used in clinical procedures. Titanium and titanium base alloys are widely use materials for implants due to their excellent mechanical properties and good biocompatibility (source). The use of gold is also frequent in multiple medical procedures, such as reconstructive surgery of the middle ear, drug delivery microchips or anti-tumor treatments among others (source). Furthermore, they have very different density properties (gold density is 19.30 g/cm3

while titanium density is 4.506 g/cm3) so we can evaluate the value of the algorithm under different situations.

3.3.2 Real data: Rodent studies

For evaluation with real data we have selected two rodent studies acquired with the ARGUS scanner. Both are rat studies from a research project on deep brain stimulation (DBS), in which the rats have electrodes down to the brain and screws on the skull (figure 3-9, left). These metallic elements cause strong metal artifact, as it can ben seen in figure 3-9, right.

The acquired projections have a matrix size of 516x570 pixels with a pixel size of 0.2 mm. The voltage and current at the source were 40 kV and 339 μA respectively. The reconstructed matrix size is 516x516x570 pixels with a voxel size of 0.122 mm.
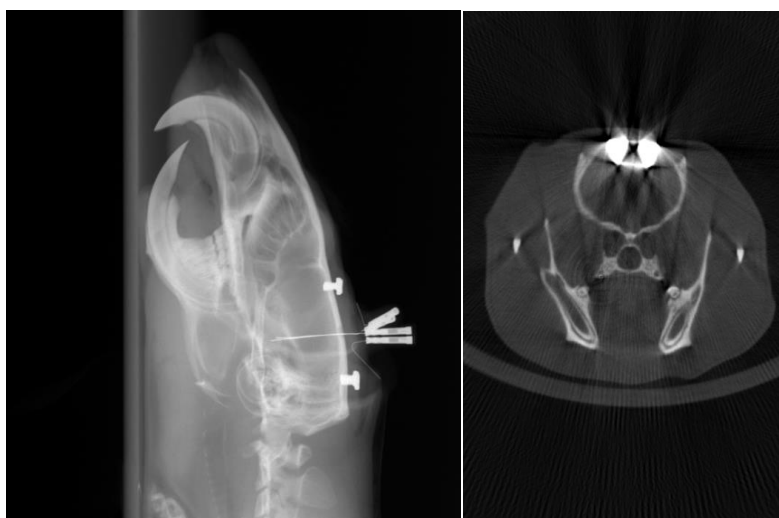
FIGURE 3-9: PROJECTION OF THE REAL DATA STUDIES DBS RAT (LEFT) AND SAGITTAL CUT (RIGHT).

3.3.3 Figures of merit

We evaluated the effectiveness of our MAR algorithm on simulated data and on real data acquired in the ARGUS scanner. Apart from visual analysis of the corrected images, we evaluate the images using the root mean square error (RMSE) and intensity profiles in an ROI affected by metallic artifact. The first part of this section details how the simulation was done. Then, the real studies are presented. Finally, the figures of merit are explained.

Root Mean Square Error

The RMSE is frequently used to measure differences between values, it is the square root of standard deviation.

In our case we will define the RMSE between the corrected and original reconstructed images with respect to a monochromatic one. This image, the monochromatic, is obtained using a monochromatic spectrum and has no metallic nor beam hardening artifact, being then a gold standard to compute the RMSE. For every simulation, we compute the RMSE for a region of interest (ROI) within the soft tissue near the metallic regions and, therefore, susceptible to metal artifacts. The equation for the RMSE is:

$$RMSE = \frac{\sqrt{\left(\sum_{i,j} I_{i,j}\right)^2 - \left(\sum_{i,j} M_{i,j}\right)^2}}{n}$$

Where n is the number of pixels, I is the original or the MAR image and M is the monochromatic image. We will compute the RMSE of the selected ROI for the original image, the image corrected for beam hardening (BH) the image corrected with MAR and the image corrected for both MAR and BH

Intensity profiles

The intensity profile of an image is the set of intensity values taken from regularly spaced points along a line segment or multiline path in an image. Comparing profile plots of original and corrected image it is possible to observe whether the streaks due to the metal artifact or beam hardening effect have been corrected. We will trace the profiles in regions of soft tissue with streak artifact, avoiding edges with bone structures, as the profiles for soft tissue are expected to be smooth. In this way, we can clearly identify profile fluctuations due to artifact in the image.

4. RESULTS

4.1 Simulated data

Figures 4-1 shows the images of each case: Single hip titanium implant, double hip titanium implant and gold inter-vertebral implant.

All MAR corrected images and the MAR+BH ones of titanium cases present a strong reduction of streak artifacts that become hardly perceptible to the eye. However, when it comes to the metallic structures, their shape is accurately identified but a black circular contour appears. Besides the edge information of bone structures in MAR images is clearly delimited with sharp edges but no so much in the MAR+BH the edges appear blurrier.

In the gold case, the high frequencies of the image, due to the great density differences between soft tissue and gold, generates artifacts when correcting beam hardening with the method of Joseph and Spital.
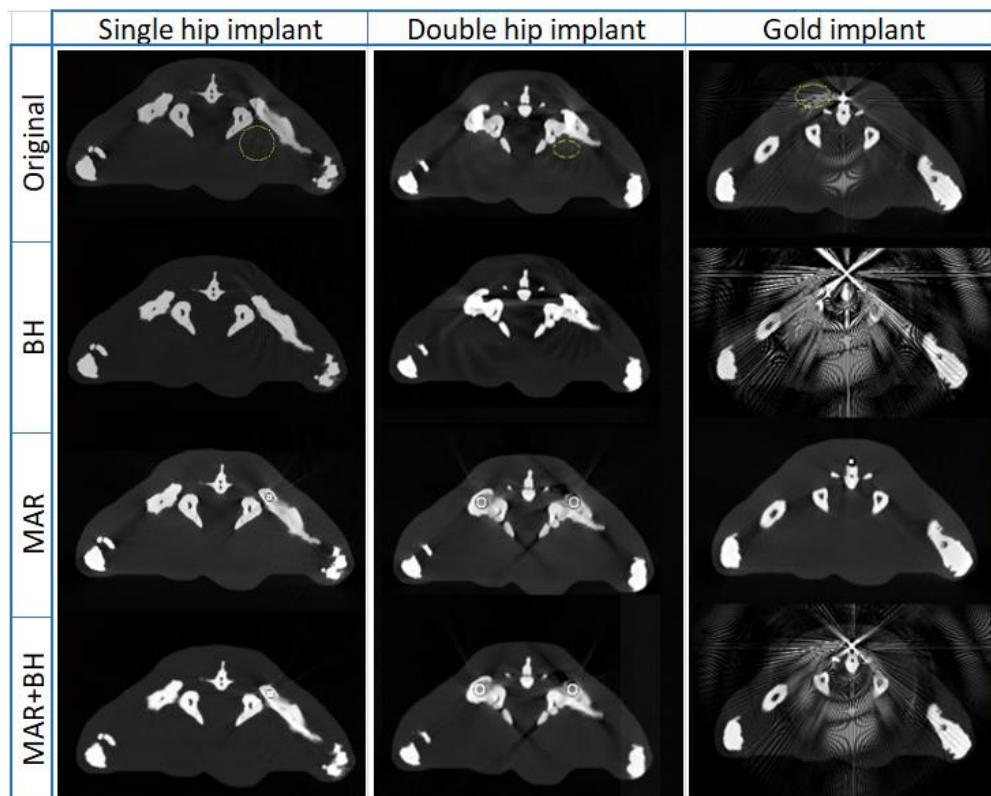
FIGURE 4.1: SIMULATED CASES IMAGES.

Table 4-1 contains the results for the mean square errors calculated:

CASE	ORIGINAL	MAR	MAR+BH	BH
SINGLE HIP IMP.	0.40144	0.3974	0.40061	0.40317
DOUBLE HIP IMP.	0.40681	0.39736	0.39845	0.4132
GOLD IMP.	0.64986	0.60509	0.67149	0.7191

TABLE 4-1: RMSE FOR A ROI IN THE SIMULATED CASE IMAGES.

All the MAR images have an RMSE smaller than their respective original image, in the gold case the difference is notably larger than for the titanium ones. This is since gold is much denser than titanium, causing a more severe artifact.

In the titanium cases, BH corrected images RMSE is larger than the originals ones, while those of MAR+BH images are comprised between the original and the MAR. The beam hardening correction seams to enhance the RMSE. This is more noticeable in the gold case, where both MAR+BH and BH images have larger RMSE than the original.

Figure 4-2 shows the region for which the intensity profiles of figure 4-3 are studied in each of the cases.
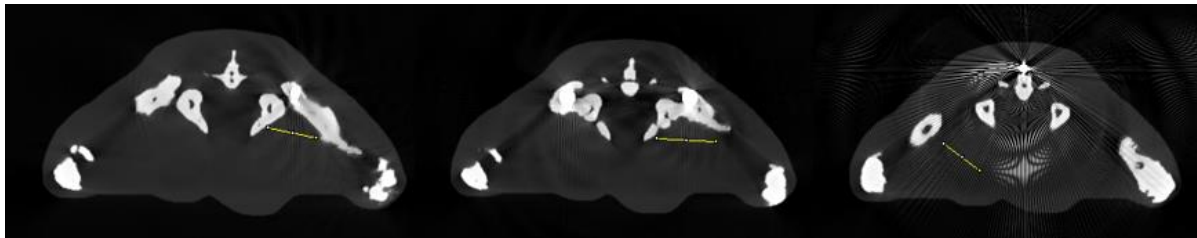
FIGURE 4-2: REGION (YELLOW) OF THE INTENSITY PROFILES PLOTTED FOR EACH CASE: (LEFT) SINGLE HIP IMPLANT (MID) DOUBLE HIP IMPLANT, (RIGHT) GOLD IMPLANT
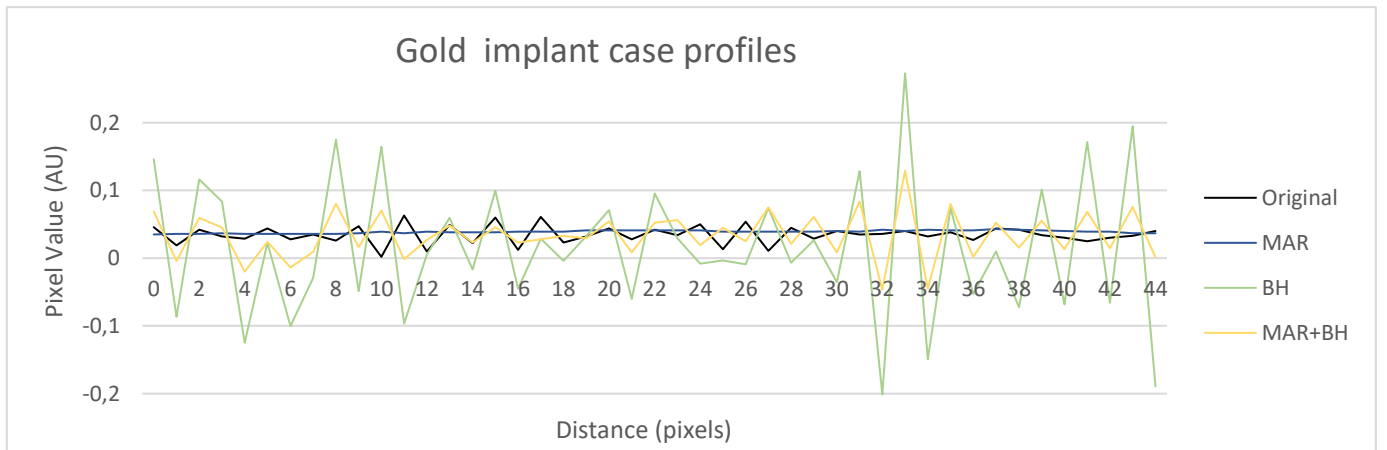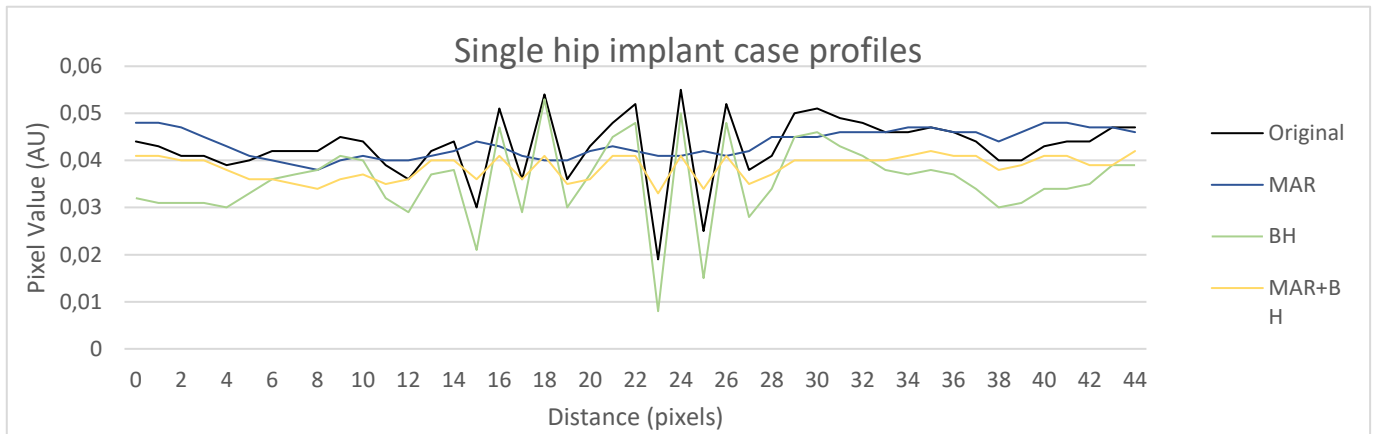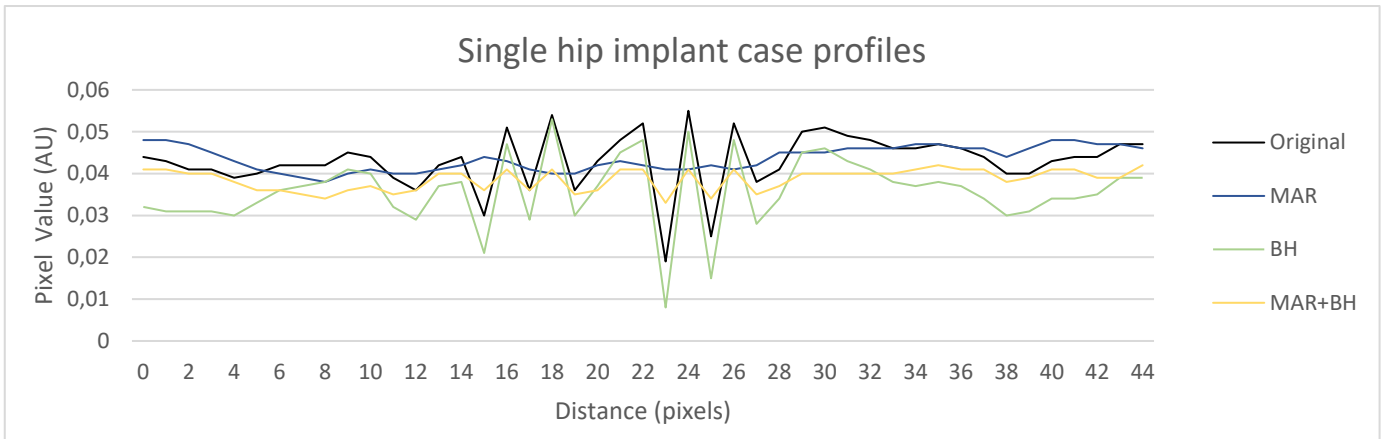
FIGURE 4-3: PROFILES OF THE SIMULATED CASES.

The first thing we notice is that all the intensity values of the corrected images are kept in the range of the original one.

In the three cases, we see that the MAR image profile presents a very flat shape compared to the original ones, in which we have strong fluctuations. The streak artifacts have been eliminated with the correction. In the gold implant profile, this difference stands out even more

although the amplitude in the plot of the original image is much bigger for gold than for the titanium ones, the resulting MAR correction achieves a similar flatness.

When it comes to the BH corrected images, for the titanium cases we see that the fluctuations present in the original images are preserved and slightly enhanced. For the gold case, the amplitude increases drastically.

The MAR+BH corrected images profiles for the titanium simulated studies present the fluctuations of the original image profile with larger amplitudes than the MAR profiles, but smaller than the original ones. In the gold case, the MAR+BH has larger fluctuations than the original, but not as large as the BH one.

4.2 Real data: Rodent studies

The images of the two real cases studied are shown in figures 4-4, the studied profiles are draw in yellow.
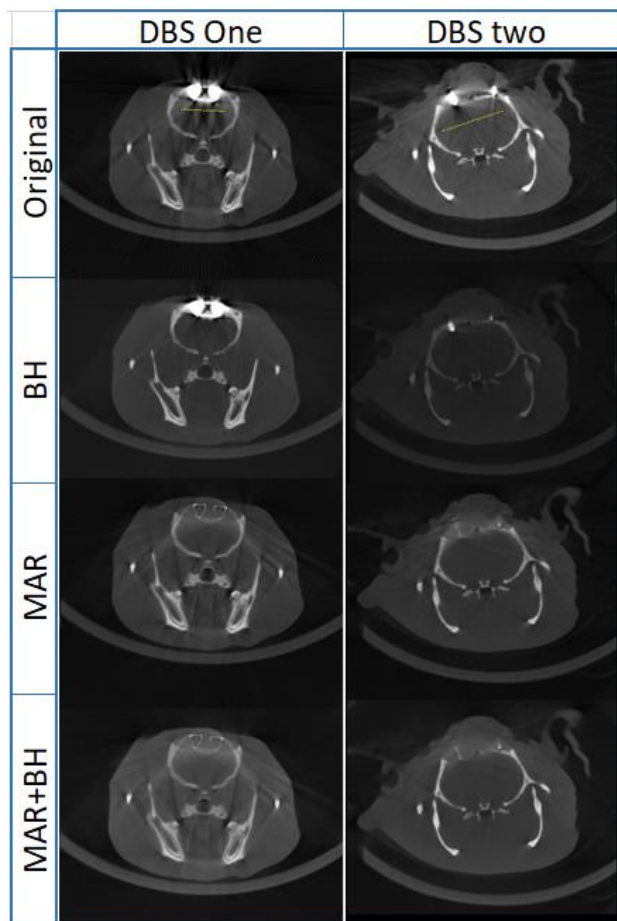
FIGURE 4-4: REAL CASES IMAGES

For both cases, the MAR and MAR+BH images present a reduction in streak artifacts and the bone edges are clearly defined. However, the metal edges are clear in the first case, but blurred in the second one. Images corrected only for BH also present a reduction in streak artifact but is less noticeable.

Figure 4-5 contains the plot of the profiles
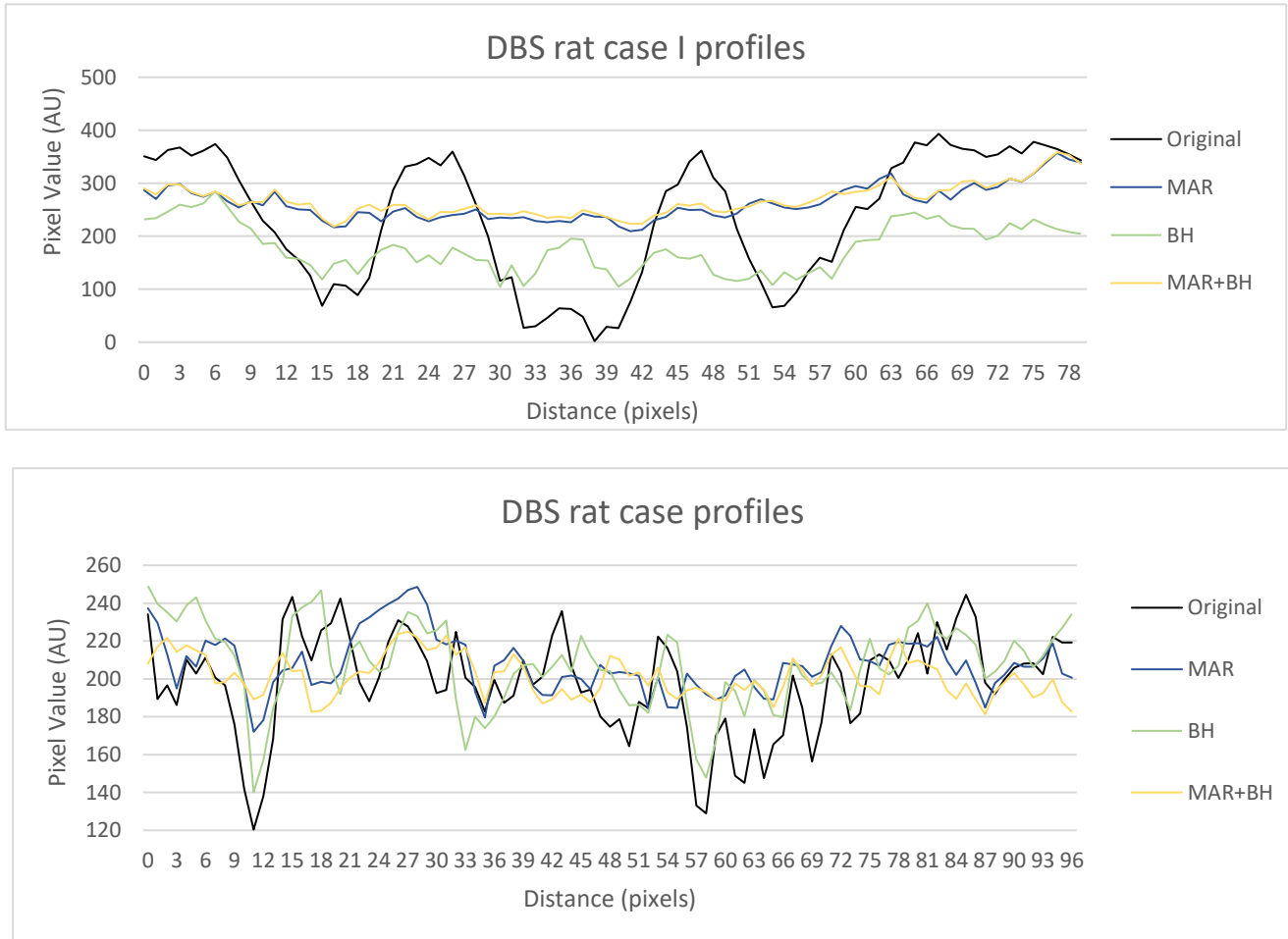
FIGURE 4-5 PROFILES OF REAL CASES.

In the first case, the fluctuations of the original image profile disappear for the MAR and the MAR+BH ones, the BH profile also has smaller fluctuations but is average value is reduced. In the second case, the deepest peaks also disappear for MAR and MAR+BH but are conserved for BH.

5. CONCLUSIONS AND FUTURE WORK

This thesis, developed with the Biomedical Imaging and Instrumentation Group of the University Carlos III de Madrid, has focused on the development of a MAR algorithm for a high-resolution micro CT.

First the physical concepts of x ray imaging and the basics of CT were reviewed, together with the study of the ARGUS scanner used and FUX-Sim, a fundamental tool for implementation of our algorithm. Next, the MAR algorithm based on the work by Meyer, using the simulator FUX-Sim was implemented in MATLAB. Finally, the MAR methods was evaluated both on simulations and real data.

The results of the evaluation show an efficient elimination of streak. The RMSE computed for a ROI containing streak artifact, with respect to the monochromatic case corroborates this result. In the three simulated cases, the obtained RMSE is smaller for the MAR corrected images than for the original one. The implemented MAR method works even for very strong artifact, as it is the case of the gold implant. In all the studies, bone edges are preserved when correcting with MAR and the metal structures are clearly delimited after correction. The tests using beam hardening correction proved that this correction is not sufficient to eliminate artifacts caused by metallic objects.

However, the method proposed has one main limitation. The segmentation step for isolating the metal structure in real studies proved to be cumbersome, since the gray values corresponding to the rat teeth in the reconstructed images happened to be in the same range than the metallic structure one. Segmentation by thresholding was not efficient, leaving part of the rat teeth in the metal image, which poses a problem as the algorithm will interpolate also these values and that would generate new artifacts. The solution was to manually correct the segmentation of the metal. Future work includes improving the segmentation step, in order to automatize it. Also, we need to perform further evaluation with real data to corroborate the preliminary results presented in this thesis. Finally, the MAR method will be integrated in the ARGUS PET/CT.

6. PROJECT MANAGEMENT

Time dedicated to the present thesis has been estimated to be 480 hours.

6.1 Personnel cost

The total personnel cost associated with the development of the present project is shown in

Table 6-1.

Category	Time (Hours)(€)	Cost/Hour(€)	Cost (€)
Biomedical engineer	480	15	7200
Project coordinator	150	35	5250
Research engineer	200	20	4000
		Total	**16450**

TABLE 6-1 PERSONNEL COST BREAKDOWN.

6.2 Materials cost

Table 6-2 displays the material used in the project with a depreciation of 20% at five years.

MATERIALS	Cost(€)	Cost/year (€)	Time (months)	Cost€)
PC	1000	800	6	400
GPU	192	153,6	6	76,8
MATLAB	6000	4800	6	2400
			Total	**2876,8**

TABLE 6-2 MATERIALS COST BREAKDOWN.

6.3 Indirect Cost

Indirect costs are calculated to be 20% of the material and human costs, which is 3865,36€.

6.4 General Cost & Industrial Benefit

General cost and industrial benefit correspond to the 16% and 6% of the material cost,

respectively. Therefore, the general cost is estimated to be 460,288 € and the industrial benefit,

172,608 €.

6.5 Total Cost

For obtaining the total cost it is necessary to add VAT which is a 21%, see table 6-3.

Concept	Cost
Personnel cost	16450
Material cost	2876,8
Indirect cost	3865,36
Total w/o VAT	23192,16
VAT(21%)	4870,35
TOTAL BUDGET	28062,51

TABLE 6-3: TOTAL COST BREAKDOWN.

GLOSSARY

AU: Arbitrary Units

BH: Beam Hardening

BIIG: Biomedical Imaging and Instrumentation Group

CT: Computed Tomography

FBP: Filtered Backprojection

FDK: Feldkamp, David and Kreis

FOV: Field Of View

GPU: Graphic Processing Unit

kV: Kilovolts

LIM: Laboratorio de Imagen Médica

MAR: Metal Artifact Reduction

PET: Positron Emission Tomography

RMSE: Root Mean Square Error

ROI: Region Of Interest

SDD: Source-Detector Distance

SOD: Source-Object Distance

VAT: Value Added Taxes

μA: Microamperes

BIBLIOGRAPHY

[1]   European Space Agency, "ESA - Science & Technology," 23 May 2012. [Online]. Available: http://sci.esa.int/jump.cfm?oid=50368. [Accessed Jul 2017].

[2]   Antonine Education, [Online]. Available: http://www.antonine-education.co.uk/Pages/Physics_5_Options/Medical_Physics/MED_07/med_phys_7.htm. [Accessed Jul 2016].

[3]   File:Old x ray tube valugi 2.jpg. (2016, November 29). *Wikimedia Commons, the free media repository.* Retrieved 08:14, July 22, 2017 from https://commons.wikimedia.org/w/index.php?title=File:Old_x_ray_tube_valugi_2.jpg&oldid=223787333.

[4]   J. Beutel, H. L. Kundel and R. L. Van Metter, Handbook of Medical Imaging: Physics and psychophysics, SPIE Press, 2000.

[5]   "Scientific Sentence," 2010. [Online]. Available: http://scientificsentence.net/Radiations/index.php?key=yes&Integer=attenuation. [Accessed Jul 2017].

[6]   M. M. Körner, C. H. M. Weber, S. M. Wirth, K.-J. M. Pfeifer, M. F. M. Reiser and M. M. Treitl, "Advances in Digital Radiography: Physical Principles and System Overview," RadioGraphics, vol. 27, no. 3, pp. 675-686, 2007.

[7]   Start Radiology, [Online]. Available: http://www.startradiology.com/the-basics/x-rayct-technique/ [Accessed Sep 2016]

[8]   M. D. and J. J. V. Abella, M, "Contributions to Image Reconstruction in High-Resolution Multimodality Systems for Preclinical Applications," 2010.

[9]   J. F. Barrett and N. Keat, "Artifacts in CT: recognition and avoidance." Radiographics, vol. 24, no. 6, pp. 1679–91, Jan. 2004.

[10]   M. Abella, J. J. Vaquero, A. Sisniega, J. Pascau, A. Udías, V. García, I. Vidal, and M. Desco, "Software architecture for multi-bed FDK-based reconstruction in X-ray CT scanners.," Comput. Methods Programs Biomed., vol. 107, no. 2, pp. 218–32, Aug. 2012.

[11]   Y. Sun, Y. Hou, F. Zhao, and J. Hu, "A calibration method for misaligned scanner geometry in cone-beam computed tomography," NDT E Int., vol. 39, no. 6, pp. 499–513, Sep. 2006.

[12]   Kak, A.C., Slaney, Malcolm, Principles of Computerized Tomographic Imaging. IEEE Press, 1988.

[13]   Wu, M., Keil, A., Constantin, D., Star-Lack, J., Zhu, L. and Fahrig, R, "Metal artifact correction for x-ray computed tomography using kV and selective MV imaging". Med. Phys., 41: n/a, 121910. doi:10.1118/1.4901551, 2014

[14]   Ballhausen H, Reiner M, Ganswindt U, Belka C, Söhn M. "Post-processing sets of tilted CT volumes as a method for metal artifact reduction". Radiat. Oncol. 9, 114. 2014.

[15]   Frédérique L., Recur B., Genot S., Domenger JP., Desbarats P. "Sinogram Restoration Using Confidence Maps to Reduce Metal Artifact in Computed Tomography." In: Campilho A., Karray F. (eds) Image Analysis and Recognition. ICIAR 2016. Lecture Notes in Computer Science, vol 9730. Springer, Cham, 2016.

[16]   Liugang, G. et al. Metal artifact reduction through MVCBCT and kVCT in radiotherapy. *Sci. Rep.* 6, 37608; doi: 10.1038/srep37608, Nov 2016.

[17]   K. Müller, S. Datta, M. Ahmad, J.-H. Choi, T. Moore, L. Pung, C. Niebler, G. E. Gold, A. Maier, and R. Fahrig, "Interventional dual-energy imaging¡a feasibility of rapid kv-switching on a c-arm CT system," Medical Physics, vol. 43, no. 10, pp. 5537–5546, 2016.

[18]   Zhang Y[1], Zhang L, Zhu XR, Lee AK, Chambers M, Dong L., "Reducing metal artifacts in cone-beam CT images by preprocessing projection data.",Int J Radiat Oncol Biol Phys. 2007 Mar 1;67(3):924-32. Epub, Dec 2006

[19]   Giantsoudi, D., De Man, B., Verburg, J., Trofimov, A., Jin, Y., Wang, G., Gjesteby, L. and Paganetti, H. "Metal artifacts in computed tomography for radiation therapy planning: dosimetric effects and impact of metal artifact reduction". *Physics in Medicine and Biology*, 62(8), pp.R49-R80. 2017.

[20]   Andersson KM, Norrman E, Geijer H, Krauss W, Cao Y, Jendeberg J, et al. "Visual grading evaluation of commercially available metal artefact reduction techniques in hip prosthesis computed tomography." Br J Radiol; 89: 20150993., 2016

[21]   Bär, E., Schwahofer, A., Kuchenbecker, S. and Häring, P. "Improving radiotherapy planning in patients with metallic implants using the iterative metal artifact reduction (iMAR) algorithm". Biomedical Physics & Engineering Express, 1(2), p.025206., 2015.

[22]   W. A. Kalender, R. Hebel, and J. Ebersberger, "Reduction of CT artifacts caused by metallic implants," Radiology, vol. 164, no. 2, pp. 576–577, Aug. 1987.

[23]   E. Meyer, R. Raupach, M. Lell, B. Schmidt, and M. Kachelrieß, "Normalized metal artifact reduction (NMAR) in computed tomography," Med. Phys. 37(10), 5482–5493, 2010.

[24]   Meyer E, Raupach R, Lell M, Schmidt B, Kachelrieß M. Frequency split metal artifact reduction (FSMAR) in computed tomography. Med Phys; 39: 1904–16. 2012.

[25]   D. Prell, Y. Kyriakou, T. Struffert, A. Do¨rfler, and W. Kalender, "Metal artifact reduction for clipping and coiling in interventional C-arm CT," Am. J. Neuroradiol. 31(4), 634–639. 2010.

[26]   J Pascau, JJ Vaquero, M Abella García, R Cacho, E Lage, M Desco, "Multimodality workstation for small animal image visualization and analysis" Springer. 2006

[27]   M Abella, JJ Vaquero, A Sisniega, J Pascau, A Udías, V García, I Vidal, "Software architecture for multi-bed FDK-based reconstruction in X-ray CT scanners", Computer methods and programs in biomedicine 107 (2), 218-232. 2012

[28]   M Abella, E Serrano, J Garcia-Blas, I García, C De Molina, J Carretero, "FUX-Sim: Implementation of a fast universal simulation/reconstruction framework for X-ray systems", PloS one 12 (7), e0180363, (2017)

[29]   B. Dogdas, D. Stout, A. Chatziioannou, RM Leahy, Digimouse: A 3D Whole Body Mouse Atlas from CT and Cryosection Data, Phys. Med. Bio, 52: 577-587, 2007.

[30]   Wikipedia contributors. "The Three Rs." *Wikipedia, The Free Encyclopedia*. Wikipedia, T The Free Encyclopedia, 23 Sep. 2017. Web.25 Sep. 2017

[31]   European Animal Research Association. "The 3Rs principles", retrieved 23 Sep. 2017, from: http://eara.eu/en/the-3rs-principles/